Four Sub-Saturns with Dissimilar Densities:
Windows into Planetary Cores and Envelopes

Erik A. Petigura[1,12], Evan Sinukoff[2,13], Eric D. Lopez[3], Ian J. M. Crossfield[4,14], Andrew W. Howard[1],
John M. Brewer[5], Benjamin J. Fulton[1,2], Howard T. Isaacson[6], David R. Ciardi[7], Steve B. Howell[8],
Mark E. Everett[9], Elliott P. Horch[10], Lea A. Hirsch[6], Lauren M. Weiss[11,15], and Joshua E. Schlieder[7]

[1] California Institute of Technology, 1200 E California Boulevard, Pasadena, CA 91125, USA; petigura@caltech.edu
[2] Institute for Astronomy, University of Hawai'i at Mānoa, 2680 Woodlawn Drive, Honolulu, HI 96822, USA
[3] Institute for Astronomy, University of Edinburgh, Blackford Hill, Edinburgh, EH9 3HJ, UK
[4] University of California, Santa Cruz, 1156 High Street, Santa Cruz, CA 95064 USA
[5] Yale University, New Haven, CT 06520, USA
[6] University of California, Berkeley, Berkeley, CA 94720, USA
[7] IPAC-NExScI, California Institute of Technology, 770 South Wilson Avenue, Pasadena, CA 91125, USA
[8] NASA Ames Research Center, Mail Stop 204-14, Moffett Field, CA 94035, USA
[9] National Optical Astronomy Observatory, 950 North Cherry Avenue, Tucson, AZ 85719, USA
[10] Department of Physics, Southern Connecticut State University, 501 Crescent Street, New Haven, CT 06515, USA
[11] Institut de Recherche sur les Exoplanètes, Université de Montréal, Canada

Abstract

We present results from a Keck/HIRES radial velocity campaign to study four sub-Saturn-sized planets, K2-27b, K2-32b, K2-39b, and K2-108b, with the goal of understanding their masses, orbits, and heavy-element enrichment. The planets have similar sizes ($R_P = 4.5$–$5.5\,R_\oplus$), but have dissimilar masses ($M_P = 16$–$60\,M_\oplus$), implying a diversity in their core and envelope masses. K2-32b is the least massive ($M_P = 16.5 \pm 2.7\,M_\oplus$) and orbits in close proximity to two sub-Neptunes near a 3:2:1 period commensurability. K2-27b and K2-39b are significantly more massive at $M_P = 30.9 \pm 4.6\,M_\oplus$ and $M_P = 39.8 \pm 4.4\,M_\oplus$, respectively, and show no signs of additional planets. K2-108b is the most massive at $M_P = 59.4 \pm 4.4\,M_\oplus$, implying a large reservoir of heavy elements of about $\approx 50\,M_\oplus$. Sub-Saturns as a population have a large diversity in planet mass at a given size. They exhibit remarkably little correlation between mass and size; sub-Saturns range from ≈ 6–$60\,M_\oplus$, regardless of size. We find a strong correlation between planet mass and host star metallicity, suggesting that metal-rich disks form more massive planet cores. The most massive sub-Saturns tend to lack detected companions and have moderately eccentric orbits, perhaps as a result of a previous epoch of dynamical instability. Finally, we observe only a weak correlation between the planet envelope fraction and present-day equilibrium temperature, suggesting that photo-evaporation does not play a dominant role in determining the amount of gas sub-Saturns accrete from their protoplanetary disks.

Key words: planets and satellites: composition – planets and satellites: detection – planets and satellites: dynamical evolution and stability – planets and satellites: formation – planets and satellites: gaseous planets – planets and satellites: interiors

Supporting material: machine-readable table

1. Introduction

The solar system contains four terrestrial planets, two ice giants, and two gas giants on nearly circular and co-planar orbits. Notably, the solar system lacks several broad classes of planets: it contains no planets having sizes between Earth and Neptune (1.0–$3.9\,R_\oplus$) or between Uranus and Saturn (4.0–$9.4\,R_\oplus$), and no planets that orbit closer than Mercury (0.39 au). A longstanding question is whether the solar system is representative of planetary systems around other stars, or if it is one particular realization of a set of physical processes that produce a diversity of outcomes.

The study of extrasolar planets offers a path to address this question. Studies of planet occurrence from the prime *Kepler* mission (Borucki et al. 2010a) revealed that our solar system is atypical in a few key ways: the majority of stars have at least one

planet interior to Mercury's orbit and the most common size of planet is in the range 1–$3\,R_\oplus$, sizes not represented in our solar system (Howard et al. 2012; Fressin et al. 2013; Petigura et al. 2013). The occurrence of planets rises rapidly below $R_P = 3.0\,R_\oplus$, indicating an important size scale in the formation of planet cores and envelopes. Constraining the bulk composition of these sub-Neptunes has been the focus of intensive radial velocity (RV) campaigns that revealed that most planets larger than $\approx 1.6\,R_\oplus$ have significant gaseous envelopes (Marcy et al. 2014; Weiss & Marcy 2014; Rogers 2015).

In this paper, we focus on another size class of planets absent in the solar system, sub-Saturns, which we define as planets having sizes between 4.0 and $8.0\,R_\oplus$. Sub-Saturns offer a superb laboratory to study planet formation history and compositions. Their large sizes require significant envelopes of H/He. For sub-Saturns, H/He comprise such a large component of the planet volume that the planets can be modeled as a high-density core with a thick H/He envelope. Measurements of the core mass fraction are simplified because details in the composition of the core have little effect on the

---

Table 1
Radial Velocities

Star	Inst.	Time	RV	σ(RV)
		BJD$_{\rm TBD}$	m s^{-1}	m s^{-1}
K2-27	HIRES	2457059.023437	−3.30	3.58
K2-27	HARPS	2457187.504940	−37782.19	2.56
K2-27	HARPS-N	2457064.713740	−37785.55	6.56
K2-27	FIES	2457045.607900	−38039.00	11.10
K2-32	HIRES	2457179.918605	2.24	1.81
K2-32	HARPS	2457185.606900	10.69	2.65
K2-32	PFS	2457198.674600	−13.95	2.31
K2-39	HIRES	2457245.118029	−2.77	1.84
K2-39	HARPS	2457255.714330	24507.93	2.66
K2-39	PFS	2457257.799090	0.73	1.64
K2-39	FIES	2457235.669620	24557.22	6.99

Note. The radial velocity (RV) measurements used in this work. We list the HIRES RVs along with other RVs from the literature, where available.

(This table is available in its entirety in machine-readable form.)

measured planet size (Lopez & Fortney 2014; Petigura et al. 2016).

Although close-in (<1 au) gaseous planets are thought to form via core accretion (Pollack et al. 1996; Bodenheimer et al. 2000; Hubickyj et al. 2005; Mordasini et al. 2008), there are major uncertainties regarding how planets acquire (and lose) mass and the extent to which their orbits evolve with time. For example, Jupiter is thought to have taken ∼3 Myr to accrete enough gas before triggering runaway accretion (Hubickyj et al. 2005), while gas disks around other stars are observed to dissipate after 1–10 Myr (Mamajek 2009). That these two processes have similar timescales may explain why the occurrence of Jovians within 20 au is ≈20% rather than ≈100% (Cumming et al. 2008).

Although sub-Saturns are similar to Jovians given their H/He envelopes, they often have much lower masses. For example, Kepler-79d is 7.2 $R_\oplus$ and only 6.0 $M_\oplus$ (Jontof-Hutter et al. 2014). For sub-Saturns, the runaway accretion of gas invoked to explain Jupiter's massive envelope seems to have not occurred. Low-density sub-Saturns have inspired alternative gas accretion scenarios, such as accretion in a gas-depleted disk (e.g., Lee & Chiang 2015).

Here, we present RV measurements of four Sub-Saturns, K2-27b, K2-32b, K2-39b, and K2-108b, taken as part of a program to expand the sample of sub-Saturns with well-measured masses and radii. These planets were observed by the *Kepler Space Telescope* (Borucki et al. 2010a) operating during its *K2* mission, where the telescope observes a new field in the ecliptic plane every ≈3 months (Howell et al. 2014). Sections 2–4 present the RV measurements, stellar characterization, and modeling needed to extract planet mass, radius, and orbital eccentricity. For these planets, we achieve mass measurements of 16% or better and density measurements to 33% or better.

In Section 5, we place the four planets in the context of other sub-Saturns. We find a large diversity in planet masses in the sub-Saturn size range with little correlation with planet size. Sub-Saturns range from ≈6 to 60 $M_\oplus$, regardless of their size. We find a strong correlation between stellar metallicity and planet mass, suggesting metal-rich disks likely form more massive planet cores. We also observe that planet mass seems to be inversely correlated with the presence of additional planets, which could be the result of a period of large-scale

dynamical instabilities resulting in mergers or scattering onto high inclination orbits. We apply the interior structure models of Lopez & Fortney (2014) to determine the fraction of planet mass in H/He and heavy element. For sub-Saturns, we see only a weak dependence of the envelope fraction on equilibrium temperature, indicating that photo-evaporation does not likely play a major role in sculpting the final sizes of sub-Saturns. We offer some concluding thoughts in Section 6.

2. RV Observations and Analysis

Here, we describe our overall RV observational campaign and our analysis methodology. Details on individual systems are given in Section 4. We observed K2-27, K2-32, K2-39, and K2-108 using the High Resolution Echelle Spectrometer (HIRES; Vogt et al. 1994) on the 10 m Keck Telescope I. We collected spectra through an iodine cell mounted directly in front of the spectrometer slit. The iodine cell imprints a dense forest of absorption lines which serve as a wavelength reference. We used an exposure meter to achieve a consistent signal to noise level for each program star, which ranged from 100 to 130 per reduced pixel on blaze near 550 nm. We also obtained a "template" spectrum without iodine.

RVs were determined using standard procedures of the California Planet Search (Howard et al. 2010) including forward modeling of the stellar and iodine spectra convolved with the instrumental response (Marcy & Butler 1992; Valenti et al. 1995). The RVs are tabulated in Table 1. We also list the measurement uncertainty of each RV point, which ranges from 1.5 to 2.0 m s^{-1} and is derived from the uncertainty on the mean RV of the ∼700 spectral chunks used in the RV pipeline.

We analyzed the RV time series using the publicly available RV-fitting package radvel (B. Fulton & E. Petigura 2017, in preparation).[16] When modeling the RVs, we adopt the likelihood, $\mathcal{L}$, of Howard et al. (2014):

$$\ln \mathcal{L} = -\frac{1}{2} \sum_i \left[\frac{(v_i - v_{m,i})^2}{\sigma_i^2 + \sigma_{\rm jit}^2} + \ln 2\pi (\sigma_i^2 + \sigma_{\rm jit}^2) \right],$$

where v_i is the ith RV measured at time t_i, σ_i is the corresponding uncertainty, v_m is the Keplerian model velocity at t_i, and $\sigma_{\rm jit}$ or "jitter" accounts for additional RV variability due to stellar and instrumental noise and is included in our models as a free parameter.

When modeling the RVs, we first consider circular Keplerians with no additional acceleration term, $\dot{\gamma}$. Here, $\sigma_{\rm jit}$ and an average RV offset, γ, are allowed to float as free parameters. We then allow for more complicated models if they are motivated by the data. We consider models where $\dot{\gamma}$ is allowed to float and models where eccentricity, e, and longitude of periastron, $\omega_\star$, are allowed to vary.[17] More complex models will naturally lead to higher likelihoods at the expense of additional free parameters. To assess whether a more complex model is justified, we use the Bayesian Information Criterion (BIC; Schwarz 1978). Models with smaller BIC, i.e., negative ΔBIC, are preferred.

When available, we incorporated RV measurements from the literature to augment our HIRES time series. RVs of K2-27, K2-32, and K2-39 have been published in Van Eylen et al.

---

[16] https://github.com/California-Planet-Search/radvel
[17] During fitting and MCMC modeling, we parametrize e and $\omega_\star$ by $\sqrt{e} \cos \omega_\star$ and $\sqrt{e} \sin \omega_\star$, as recommended by Eastman et al. (2013), to guard against the Lucy–Sweeney bias toward non-zero eccentricities.

Table 2
K2-39 Stellar Parameters

	This Work	V16
$T_{\rm eff}$ (K)	4912 ± 60	4881 ± 20
$\log g$ (dex)	3.58 ± 0.05	3.44 ± 0.07
[Fe/H] (dex)	0.43 ± 0.04	0.32 ± 0.04
$M_\star$ ($M_\odot$)	$1.192^{+0.085}_{-0.070}$	$1.35^{+0.04}_{-0.03}$
$R_\star$ ($R_\odot$)	2.93 ± 0.21	$3.90^{+0.30}_{-0.27}$
Parallax (mas)[a]	$3.50^{+0.24}_{-0.20}$	2.62 ± 0.20

Note. Comparison of the stellar properties from this work (based on SME; Brewer et al. 2015) and from Van Eylen et al. (2016a). $M_\star$ and $R_\star$ in the Van Eylen et al. (2016a) column were derived using the isochrones package, which interpolates among the Dartmouth isochrones, as opposed to Van Eylen et al. (2016a), who used Yonsei–Yale isochrones. However, Van Eylen et al. (2016a) gives $R_\star = 3.88^{+0.48}_{-0.42}\ R_\odot$, which is consistent with the Dartmouth model. We adopt the SME value given that the code has been extensively tested against asteroseismology.
[a] Implied parallax from based on spectroscopic properties, isochrone modeling, and apparent K-band magnitude.

(2016b), Dai et al. (2016), and Van Eylen et al. (2016a), respectively, and include RV measurements from the following instruments: FIES (Telting et. al 2014), HARPS-N (Cosentino et al. 2012), HARPS (Mayor et. al 2003), and PFS (Crane et al. 2010). We fit for the offset and jitter terms independently for different data sets. To derive uncertainties on the RV parameters, we perform a standard MCMC exploration of the likelihood surface using the emcee Python package (Goodman & Weare 2010; Foreman-Mackey et al. 2013). In Tables 3–6, we list orbital and planetary properties assuming both circular and eccentric orbits. The preferred model is indicated.

3. Stellar Properties

We measured stellar effective temperature $T_{\rm eff}$, surface gravity $\log g$, and metallicity [Fe/H], from our iodine-free "template" spectra. We followed the methodology of Brewer et al. (2016), which used an updated version of the SME code and has been shown to recover surface gravities consistent with those from asteroseismology to within 0.05 dex (Brewer et al. 2015). We constrained stellar mass $M_\star$, radius $R_\star$, and age from $T_{\rm eff}$, $\log g$, and [Fe/H] using the isochrones Python package (Morton 2015), which interpolates among the Dartmouth stellar isochrones (Dotter et al. 2008). The stellar properties are listed alongside other system properties in Tables 3–6, respectively.

For K2-39, we note some tension between the stellar parameters presented by Van Eylen et al. (2016a) and those presented here. Importantly, the $\log g$ derived by Van Eylen et al. (2016a) is lower than the SME value. The Van Eylen et al. (2016a) analysis resulted in a larger inferred stellar radius measurement that, at $R_\star = 3.90^{+0.30}_{-0.27}\,R_\odot$, is 34% larger than the $R_\star = 2.93 \pm 0.21\,R_\odot$ derived by SME and isochrones. We present a side-by-side comparison of the spectroscopic parameters in Table 2.

Can the recently released *Gaia* parallaxes be used to resolve these different estimates of stellar radius? K2-39 is listed in the Tycho catalog as TYC-5811-835-1. *Gaia* recently released parallaxes for most stars in the two-million-star Tycho catalog. K2-39 has a parallax of 3.35 ± 0.86 mas. Given the apparent K-band magnitude of 8.516 ± 0.024 from 2MASS (Cutri et al. 2003), we calculated the parallax implied by both sets of spectroscopic parameters. We used K-band since it is less

sensitive to the unknown amount of extinction between Earth and K2-39. When we used the SME parameters we found a parallax of $3.50^{+0.24}_{-0.20}$ mas, in close agreement with the *Gaia* parallax. The larger radius of Van Eylen et al. (2016a) necessitates a more distant star to produce the observed K mag, and thus yields a smaller expected parallax of 2.62 ± 0.20 mas. Although this parallax is smaller than the most likely *Gaia* value, it is still consistent at the 1σ level. Given that *Gaia* Data Release 1 provided a 4σ measurement of K2-39's parallax, it is insufficient to distinguish between the two sets of parameters. Future *Gaia* releases will provide important constraints on the physical properties of K2-39.

Van Eylen et al. (2016a) also noted that the non-detection of asteroseismic modes places a lower limit of $\log g \geqslant 3.50$ dex. Taken together, the non-detection of asteroseismic modes and the *Gaia* parallax both suggest that K2-39 is smaller than reported in Van Eylen et al. (2016a). Given that SME has been extensively tested against asteroseismology, we adopt the SME parameters hereafter.

4. Individual Targets

4.1. K2-27

K2-27 hosts a single transiting sub-Saturn, K2-27b, with $P = 6.77$ days that was first confirmed in Van Eylen et al. (2016b) using RVs. We obtained 15 spectra of K2-27 with HIRES between 2015 February 5 and 2016 July 17. Van Eylen et al. (2016b) observed this star with HARPS, HARPS-N, and FIES. We included 6 and 19 measurements from HARPS and HARPS-N, respectively in our RV analysis. We did not include the six FIES measurements because their uncertainties are much larger ($\approx 30\,{\rm m\,s^{-1}}$), compared to uncertainties from the HIRES, HARPS, and HARPS-N spectra (≈ 4–$5\,{\rm m\,s^{-1}}$), and hence add little additional information to constrain the RV fits while increasing model complexity.

We first modeled the combined RVs assuming circular orbits and no additional acceleration term, $\dot{\gamma}$. We then allowed $\dot{\gamma}$ to vary, but found that these models produced a negligible improvement in the BIC ($\Delta{\rm BIC} = -1$). We then allowed for eccentricity to float and found a non-zero eccentricity of $e = 0.251 \pm 0.088$. Compared to the circular models, the eccentric fits were strongly favored ($\Delta{\rm BIC} = -14$). We verified that the eccentricity is detected in both HIRES and HARPS+HARPS-N data sets by fitting these subsets independently. These data sets yield consistent and non-zero eccentricities. We adopted the parameters from the eccentric model as the preferred parameters. The most probable eccentric model is shown in Figure 1. The K2-27 system parameters are summarized in Table 3. We measured a Doppler semi-amplitude of $K = 11.8 \pm 1.8\,{\rm m\,s^{-1}}$, which is consistent with $K = 10.8 \pm 2.7\,{\rm m\,s^{-1}}$ reported by Van Eylen et al. (2016b), but with smaller uncertainties, due to our additional measurements. We measured a mass of $M_{\rm P} = 30.9 \pm 4.6\,M_\oplus$ and a density of $1.87 \pm 0.41\,{\rm g\,cm^{-3}}$. As we discuss in Section 5, K2-27b has a relatively high mass for its size, implying a large core mass.

4.2. K2-32

K2-32 hosts three planets, K2-32b, K2-32c, and K2-32d, having orbital periods of $P = 8.99$ days, 20.66 days, and 31.7 days, respectively, which are near the 3:2:1 period commensurability. The planets were first confirmed in Sinukoff et al. (2016) using
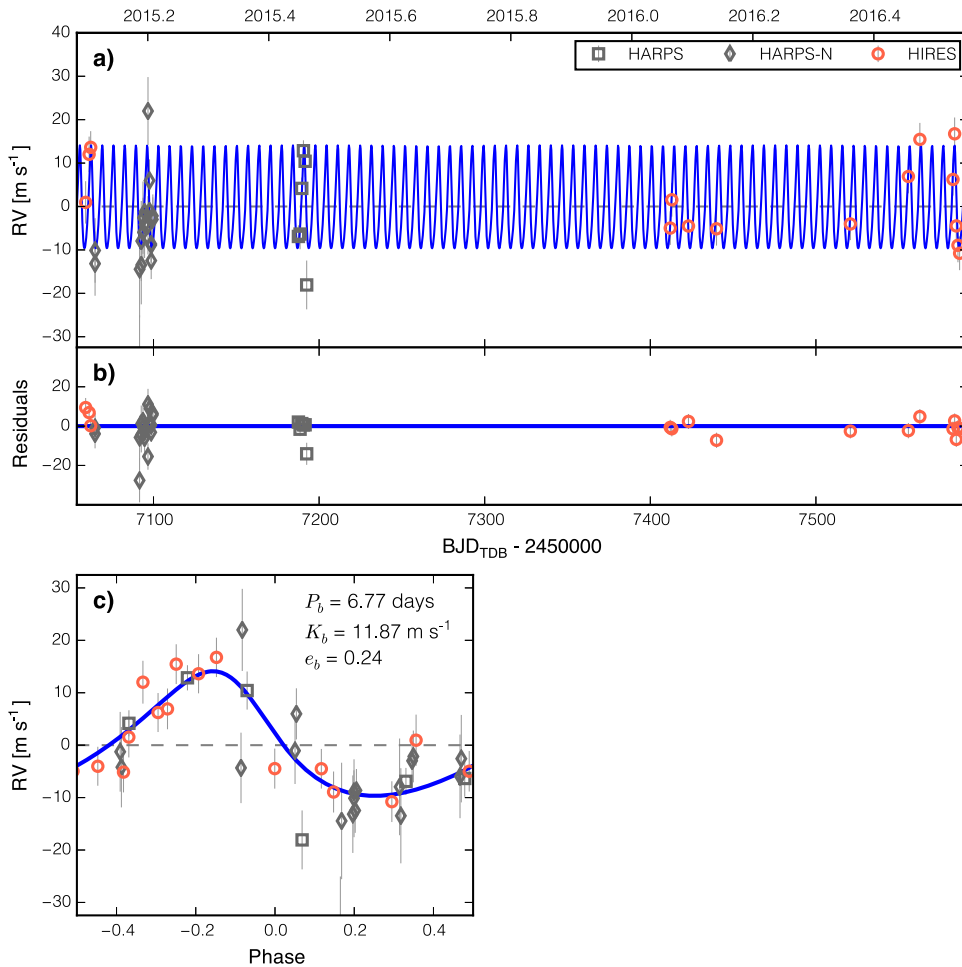
Figure 1. Single Keplerian model of K2-27 radial velocities (RVs), allowing for eccentricity (see Section 4.1). (a) Time series of RVs from HIRES along with HARPS and HARPS-N published in Van Eylen et al. (2016b). During the fitting, we allowed for an arbitrary offset between the three instruments to float as a free parameter. The blue line shows the most probable Keplerian model. (b) Residuals to the most probable Keplerian model. (c) Phase-folded RVs and the most probable Keplerian.

multiplicity arguments (Lissauer et al. 2012). We obtained 31 spectra of K2-32 with HIRES between 2015 June 06 and 2016 August 20. Dai et al. (2016) obtained 43 spectra with HARPS and 6 with PFS, which we included in our RV analysis. We first modeled the combined HIRES, HARPS, and PFS RVs assuming circular orbits and no additional acceleration term, $\dot{\gamma}$. When allowing $\dot{\gamma}$ to float, we found that $\dot{\gamma} = 2.3 \pm 1.8 \, \mathrm{m \, s^{-1} \, yr^{-1}}$, consistent with zero at the 2σ level. This differs from $\dot{\gamma} = 34.0^{+9.9}_{-9.7} \, \mathrm{m \, s^{-1} \, yr^{-1}}$ reported by Dai et al. (2016). All but five of the RVs from Dai et al. (2016) were collected within a 25 day window, and thus do not provide much leverage on $\dot{\gamma}$. The positive $\dot{\gamma}$ measured by Dai et al. (2016) is driven by two RV measurements that fall above our best-fit curve. With our combined data set spanning two observing seasons, we place tighter limits on $\dot{\gamma}$ and on the presence of long-period companions having $P \gtrsim 2$ years. Nonetheless, the BIC preferred fixing $\dot{\gamma}$ at $0 \, \mathrm{m \, s^{-1} \, yr^{-1}}$ ($\Delta\mathrm{BIC} = 1$).

Next, we considered eccentric models. In the circular models, $K_\mathrm{b} = 1.6 \pm 1.0 \, \mathrm{m \, s^{-1}}$ and $K_\mathrm{c} = 2.3 \pm 1.1 \, \mathrm{m \, s^{-1}}$. Given that the reflex motion due to K2-32c and K2-32d were only detected at the 2σ level, we cannot place meaningful constraints on their eccentricities. Therefore, we fixed their eccentricities at zero in our fits and allowed the eccentricity of K2-32b to float. We found that the eccentricity of K2-32b was

consistent with zero, and placed an upper limit of $e_\mathrm{b} < 0.23$ (95% conf.). We therefore adopted the circular model for the K2-32 system parameters. The physical properties of the K2-32 system along with our circular and eccentric models are listed Table 4. The best-fit circular model is shown in Figure 2.

For K2-32b, we measured $M_\mathrm{P} = 16.5 \pm 2.7 \, M_\oplus$, which is lower than, but within, the 1σ confidence interval of $M_\mathrm{P} = 21.1 \pm 5.9$, measured by Dai et al. (2016). We measure a density of $\rho = 0.67 \pm 0.16 \, \mathrm{g \, cm^{-3}}$, which is low compared to other sub-Saturns of similar size with RV mass measurements. However, when compared to the ensemble of mass measurements from TTVs and RVs, K2-32b is of intermediate density (see Section 5).

Figure 2 shows that the Dai et al. (2016) measurements were not well-sampled during the quadrature times of K2-32c and K2-32d, leading to poor constraints on their Doppler semi-amplitudes with significant covariance between K_c and K_d due the 3:2 period ratios of the planets. Our combined data set has more uniform sampling in phase with minimal covariance between K_c and K_d.

We achieve marginal detections of K2-32c and K2-32d, which have masses of $6.2 \pm 3.9 \, M_\oplus$ and $10.3 \pm 4.7 \, M_\oplus$, respectively. Because K2-32c is not quite a 2σ detection, we conservatively report an upper limit of $M_\mathrm{P} < 12.1 \, M_\oplus$ (95%

Table 3
System Parameters of K2-27

	Value	Reference
Stellar Parameters		
Identifier	EPIC-201546283	
$T_{\rm eff}$ (K)	5248 ± 60	A
$\log g$ (dex)	4.48 ± 0.05	A
[Fe/H] (dex)	0.13 ± 0.04	A
$v \sin i$ (km s^{-1})	2.3	A
$M_\star$ ($M_\odot$)	$0.866^{+0.029}_{-0.023}$	A
$R_\star$ ($R_\odot$)	0.885 ± 0.043	A
age (Gyr)	$10.3^{+3.3}_{-5.2}$	A
Apparent V (mag)	12.64 ± 0.02	A
Planet b		
Transit Model		
P (days)	6.771315 ± 0.000085	B
T_0 (BJD-2454833)	1979.84484 ± 0.00057	B
$R_{\rm P}$ ($R_\oplus$)	4.48 ± 0.23	A
a (au)	0.06702 ± 0.00071	A
$S_{\rm inc}$ ($S_\oplus$)	116^{+16}_{-12}	A
$T_{\rm eq}$ (K)	902 ± 28	A
Circular RV Model		
K (m s^{-1})	9.9 ± 2.0	A
$\gamma_{\rm HIRES}$ (m s^{-1})	-2.7 ± 2.0	A
$\gamma_{\rm HARPS}$ (m s^{-1})	-0.3 ± 3.8	A
$\gamma_{\rm HARPS-N}$ (m s^{-1})	6.4 ± 2.2	A
$\dot{\gamma}$ (m s^{-1} yr^{-1})	0 (fixed)	A
$\sigma_{\rm jit,HIRES}$ (m s^{-1})	$6.1^{+2.0}_{-1.4}$	A
$\sigma_{\rm jit,HARPS}$ (m s^{-1})	$6.9^{+5.9}_{-3.2}$	A
$\sigma_{\rm jit,HARPS-N}$ (m s^{-1})	4.7 ± 2.4	A
$M_{\rm P}$ ($M_\oplus$)	26.7 ± 5.3	A
ρ (g cm^{-3})	1.61 ± 0.42	A
Eccentric RV Model (Adopted)		
K (m s^{-1})	11.8 ± 1.8	A
e	0.251 ± 0.088	A
$\gamma_{\rm HIRES}$ (m s^{-1})	-2.2 ± 1.6	A
$\gamma_{\rm HARPS}$ (m s^{-1})	0.2 ± 2.7	A
$\gamma_{\rm HARPS-N}$ (m s^{-1})	6.4 ± 2.2	A
$\dot{\gamma}$ (m s^{-1} yr^{-1})	0 (fixed)	A
$\sigma_{\rm jit,HIRES}$ (m s^{-1})	$4.4^{+1.8}_{-1.2}$	A
$\sigma_{\rm jit,HARPS}$ (m s^{-1})	$4.1^{+4.8}_{-2.6}$	A
$\sigma_{\rm jit,HARPS-N}$ (m s^{-1})	$4.8^{+2.6}_{-2.1}$	A
$M_{\rm P}$ ($M_\oplus$)	30.9 ± 4.6	A
ρ (g cm^{-3})	1.87 ± 0.41	A

Note. A: this work; B: Crossfield et al. (2016).

confidence) to be conservative. Continued Doppler monitoring of K2-32 is necessary to place tighter constraints on the masses and orbits of K2-32c and K2-32d. Although such observations are challenging with current instruments given the faint host star ($V = 12.3$ mag), the dynamical richness of this system makes these observations worthwhile.

4.3. K2-39

K2-39 hosts a single transiting planet, K2-39b, with $P = 4.60$ days, which was first confirmed by Van Eylen et al. (2016a). When fitting the photometry, Van Eylen et al. (2016a) and Crossfield et al. (2016) arrived at different values of the planet-to-star radius ratio, $R_{\rm P}/R_\star$, of $1.93 \pm 0.1\%$ and $2.52 \pm 0.27\%$, respectively. The Crossfield et al. (2016) solution favored a

grazing impact parameter of $b = 1.10^{+0.07}_{-0.09}$ and is responsible for the larger inferred radius ratio. Motivated by this discrepancy, we re-examined the K2-39 photometry produced by the k2phot pipeline[18] and two other publicly available light curves produced by the k2sff and k2sc pipelines (Vanderburg & Johnson 2014; Aigrain et al. 2015). For each light curve, we masked out the in-transit points and modeled the out-of-transit photometry with a Gaussian Process (Rasmussen & Williams 2005) using a squared-exponential kernel with a correlation length of 2 days. We then performed a standard MCMC exploration of the likelihood surface using the batman (Kreidberg 2015) and emcee Python packages to map out parameter uncertainties and covariances. Figure 3 summarizes the results of these different fits. The k2phot, k2sc, and k2sff light curves yielded $R_{\rm P}/R_\star$ of $1.85^{+0.15}_{-0.05}\%$, $1.76^{+0.15}_{-0.06}\%$, and $1.66^{+0.12}_{-0.05}\%$, respectively. We also note the significant correlation between $R_{\rm P}/R_\star$ and b at large values of b, which is responsible for the rather asymmetric uncertainties. Because $R_{\rm P}/R_\star$ differs by 2σ–3σ among the different reductions, we combined the three sets of MCMC chains and adopt $R_{\rm P}/R_\star = 1.79 \pm 0.13\%$ as an intermediate value of the planet-to-star radius ratio with more conservative errors.

We obtained 42 spectra of K2-39 with HIRES between 2015 August 10 and 2016 August 21. Van Eylen et al. (2016a) obtained 7 spectra with HARPS, 6 with PFS, and 17 with FIES, which we included in our analysis. In contrast to our K2-27 analysis (Section 4.1), we included FIES RVs because of the larger number of measurements (17 as opposed to 6 for K2-27) and because they are the only non-HIRES data set with a sufficient time baseline to resolve a long timescale activity signal, which we discuss below.

The RVs exhibited a large amplitude variability that was not associated with K2-39b that motivated searches for additional non-transiting planets. Figure 4 shows three successive Keplerian searches in the K2-39 RVs using a modified version of the Two-dimensional Keplerian Lomb–Scargle (2DKLS) periodogram (O'Toole et al. 2009; Howard & Fulton 2016). We observed a peak in the periodogram at $P = 4.6$ days, which corresponds to the period of K2-39b. When we measured the change in χ^2 (periodogram power) between a one-planet fit and a two-planet fit, then between a two-planet model and a three-planet model (lower two panels in Figure 4) we found several peaks that fall above the 10% empirical false alarm threshold (eFAP; Howard & Fulton 2016). However, inspection of the S-values (Isaacson & Fischer 2010; see Figure 4), which can correlate with stellar activity that can lead to spurious Doppler signals, showed significant long-term variability that is associated with the RV peak seen at ≈ 330 days and is likely not associated with another planet. We modeled out the activity signal to search for additional non-transiting planets. As a matter of convenience, we modeled the activity signature as a Keplerian and removed it from the time series. A subsequent search of the residual RVs revealed no other significant signals.

We modeled the combined HIRES, HARPS, FIES, and PFS RVs using two Keplerians: one for K2-39b and one as a convenient description of the stellar activity. We first assumed circular orbits and no additional acceleration term, $\dot{\gamma}$. We found that models that included $\dot{\gamma}$ were not favored by the BIC and fixed $\dot{\gamma} = 0$ m s^{-1} yr^{-1} in subsequent fits. Next, we allowed the eccentricity of K2-39b to float, and found that this model was preferred over the circular model (ΔBIC $= -7$). We adopted

---

<div align="center">

Table 4
K2-32 System Parameters

</div>

	Value			Reference
Stellar Parameters				
Identifier	EPIC-205071984			
$T_{\rm eff}$ (K)	5275 ± 60			A
$\log g$ (dex)	4.49 ± 0.05			A
[Fe/H] (dex)	-0.02 ± 0.04			A
$v \sin i$ (km s^{-1})	0.7			A
$M_\star$ ($M_\odot$)	0.856 ± 0.028			A
$R_\star$ ($R_\odot$)	$0.845^{+0.044}_{-0.035}$			A
age (Gyr)	7.9 ± 4.5			A
Apparent V (mag)	12.31 ± 0.02			A
	Planet b	*Planet c*	*Planet d*	
Transit Model				
P (days)	8.99213 ± 0.00016	20.6602 ± 0.0017	31.7154 ± 0.0022	B
T_0 (BJD-2454833)	2076.91832 ± 0.00055	2128.4067 ± 0.0032	2070.7901 ± 0.0026	B
$R_{\rm P}$ ($R_\oplus$)	5.13 ± 0.28	3.01 ± 0.25	3.43 ± 0.35	A
a (au)	0.08036 ± 0.00088	0.1399 ± 0.0015	0.1862 ± 0.0020	A
$S_{\rm inc}$ ($S_\oplus$)	$77.7^{+10.8}_{-8.3}$	$25.6^{+3.6}_{-2.7}$	$14.5^{+2.0}_{-1.5}$	A
$T_{\rm eq}$ (K)	817 ± 25	619 ± 19	537 ± 16	A
Circular RV Model (Adopted)				
K (m s^{-1})	5.63 ± 0.91	1.6 ± 1.0	2.3 ± 1.1	A
$\gamma_{\rm HIRES}$ (m s^{-1})	-1.69 ± 0.85			A
$\gamma_{\rm HARPS}$ (m s^{-1})	1.07 ± 0.84			A
$\gamma_{\rm PFS}$ (m s^{-1})	-6.7 ± 3.2			A
$\dot{\gamma}$ (m s^{-1} yr^{-1})	0 (fixed)			A
$\sigma_{\rm jit,HIRES}$ (m s^{-1})	$3.77^{+0.81}_{-0.65}$			A
$\sigma_{\rm jit,HARPS}$ (m s^{-1})	4.13 ± 0.73			A
$\sigma_{\rm jit,PFS}$ (m s^{-1})	$6.5^{+4.3}_{-2.4}$			A
$M_{\rm P}$ ($M_\oplus$)	16.5 ± 2.7	<12.1 (95% conf.)	10.3 ± 4.7	A
ρ (g cm^{-3})	0.67 ± 0.16	<2.7 (95% conf.)	$1.38^{+0.92}_{-0.67}$	A
Eccentric RV Model				
K (m s^{-1})	5.60 ± 0.93	1.7 ± 1.0	2.4 ± 1.1	A
e	<0.23 (95% conf.)	Unconstrained	Unconstrained	A
$\gamma_{\rm HIRES}$ (m s^{-1})	-1.70 ± 0.87			A
$\gamma_{\rm HARPS}$ (m s^{-1})	1.15 ± 0.85			A
$\gamma_{\rm PFS}$ (m s^{-1})	-6.7 ± 3.4			A
$\dot{\gamma}$ (m s^{-1} yr^{-1})	0 (fixed)			A
$\sigma_{\rm jit,HIRES}$ (m s^{-1})	$3.88^{+0.82}_{-0.65}$			A
$\sigma_{\rm jit,HARPS}$ (m s^{-1})	4.13 ± 0.73			A
$\sigma_{\rm jit,PFS}$ (m s^{-1})	$6.6^{+4.6}_{-2.5}$			A
$M_{\rm P}$ ($M_\oplus$)	16.5 ± 2.8	<12.7 (95% conf.)	10.9 ± 4.9	A
ρ (g cm^{-3})	$0.58^{+0.16}_{-0.13}$	<2.5 (95% conf.)	$1.29^{+0.86}_{-0.61}$	A

Note. A: this work; B: Crossfield et al. (2016). Because the 2σ confidence interval on $K_{\rm c}$ includes zero, we report upper limits on the mass and density of K2-32.

the eccentric model, which is shown in Figure 5. The properties of the K2-39 system are listed in Table 5.

For K2-39b, we found a mass of $M_{\rm P} = 39.8 \pm 4.4\,M_\oplus$, which agrees with $M_{\rm P} = 50.3^{+9.7}_{-9.4}\,M_\oplus$ reported by Van Eylen et al. (2016a) at the 1σ level. The additional RVs improved the precision of the mass measurement by roughly a factor of two. Our derived planet radius of $R_{\rm P} = 5.71 \pm 0.63\,R_\oplus$ is substantially smaller than $R_{\rm P} = 8.2 \pm 1.1\,R_\oplus$ reported by Van Eylen et al. (2016a). This is largely due to the smaller stellar radius (see Section 3). Our adopted value of $R_{\rm P}/R_\star = 1.79 \pm 0.13\%$ is also smaller than the Van Eylen et al. (2016a) value of $R_{\rm P}/R_\star = 1.93 \pm 0.1\%$. Although the difference in $R_{\rm P}/R_\star$ is not as large in a fractional sense as the difference in $R_\star$, it also contributes to a smaller derived $R_{\rm P}$. Thus, our derived density of $\rho = 1.17^{+0.47}_{-0.32}\,{\rm g\,cm^{-3}}$ is significantly larger than $\rho = 0.50^{+0.29}_{-0.17}\,{\rm g\,cm^{-3}}$, reported by Van Eylen et al. (2016a).

4.4. K2-108

K2-108, listed as EPIC-211736671 in the Ecliptic Planet Input Catalog (Huber et al. 2016), is a $V = 12.3$ mag star observed during *K2* Campaign 5. We identified K2-108 as a likely planet according to our team's standard methodology, described in detail in Crossfield et al. (2016). In brief, we identified a set of transits having $P = 4.73$ days and elevated K2-108 to the status of "planet candidate." We fit the light curve according to standard procedures and show the best-fitting model light curve in Figure 6. Follow-up spectroscopic observations revealed that K2-108 is a metal-rich ([Fe/H] $= 0.33 \pm 0.04$ dex), slightly evolved G star having a radius of $R_\star = 1.75 \pm 0.14\,R_\odot$. The spectroscopically determined stellar parameters along with the results from our light-curve fitting are listed in Table 6.
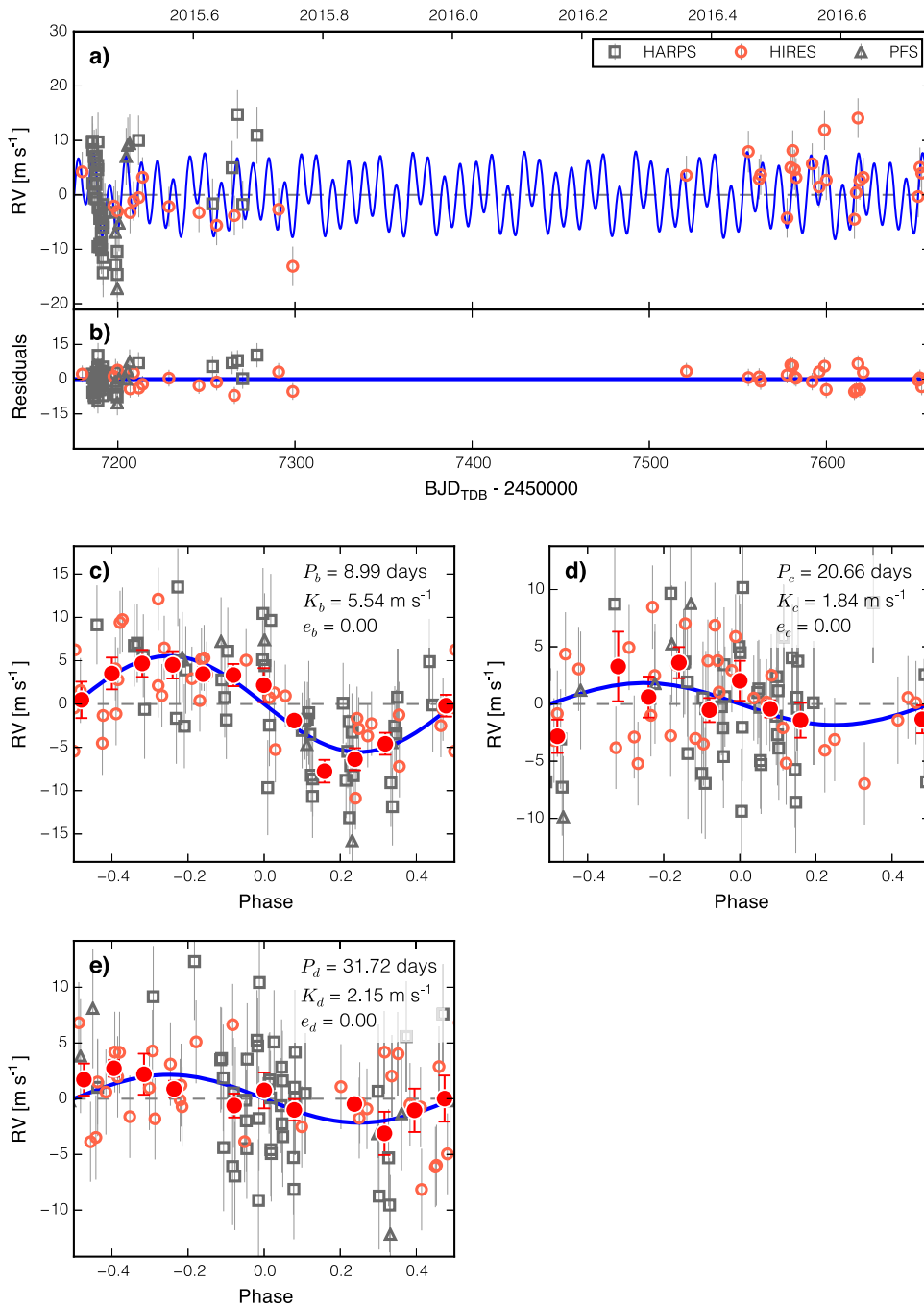
Figure 2. Three-planet Keplerian fit to the K2-32 radial velocities (RVs), assuming circular orbits (see Section 4.2). (a) Time series of RVs from HIRES along with HARPS and PFS published in Dai et al. (2016). During the fitting, we allowed for an arbitrary offset between the three instruments to float as a free parameter. The blue line shows the most probable Keplerian model. (b) Residuals to the most probable Keplerian model. Panels (c) through (e) show the phase-folded RVs and the most probable Keplerian with the contributions from the other planets removed. The large red circles show the phase-binned RVs.

We obtained 20 spectra of K2-108 with HIRES between 2015 December 23 and 2016 November 25. We first considered circular models with no acceleration term, $\dot{\gamma}$. We found that eccentric models with non-zero $\dot{\gamma}$ (shown in Figure 7) were favored over circular models ($\Delta\mathrm{BIC} = -25$). The parameters are summarized in Table 6. At $59.4 \pm 4.4\,M_\oplus$, K2-108b is remarkably massive for a $5.28 \pm 0.54\,R_\oplus$ planet, implying a large heavy-element component.

Although our RV analysis verified the planetary nature of the transiting object, we assessed the possibility of additional stellar companions in the photometric aperture that could appreciably dilute the observed transit, resulting in an incorrectly derived planetary radius. From the light curve fits, the planet-to-star radius ratio is $R_\mathrm{P}/R_\star = 2.82 \pm 0.17\%$. For an additional star to significantly alter the observed transit depth requires a flux ratio, $F_2/F_1 \approx \sigma\left((R_\mathrm{P}/R_\star)^2\right)/(R_\mathrm{P}/R_\star)^2 \approx 0.10$, or $\Delta V \approx 2.5$ mag (Ciardi et al. 2015).

A search for secondary spectral lines in the HIRES template spectrum (Kolbl et al. 2015) revealed no additional stellar companions having $\Delta V \lesssim 5$ mag and $\Delta\mathrm{RV} \gtrsim 15\,\mathrm{km\,s^{-1}}$, corresponding to a physical separation of $\lesssim 1$ au.
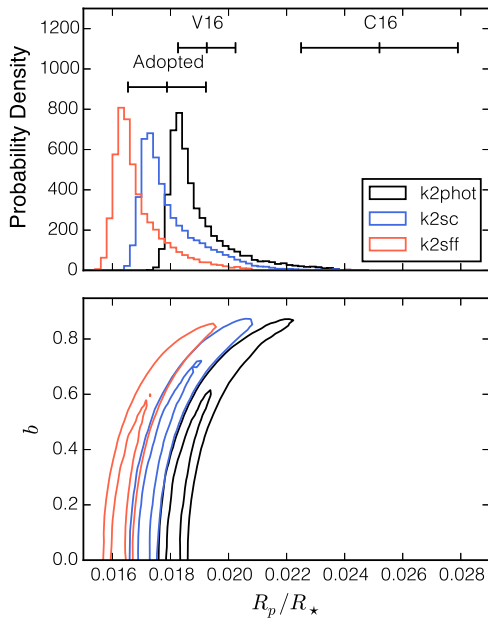
Figure 3. Results from MCMC fitting of different photometric reductions of the K2-39 light curve, described in Section 4.3. Top: different values of $R_{\rm P}/R_\star$ from the literature and this work. Significant disagreement between the Van Eylen et al. (2016a) and Crossfield et al. (2016) values (V16 and C16, respectively), motivated a reanalysis of photometry generated by three independent pipelines: k2phot, k2sc, and k2sff. The histograms show the posterior distributions after an MCMC exploration for different data sets. The different reductions led to posteriors on $R_{\rm P}$ and b that differed by $\approx 1\sigma$–3σ, perhaps due to different susceptibilities to correlated noise. Our adopted value combines all three chains to conservatively represent $R_{\rm P}/R_\star$. Bottom: the 1σ and 2σ contours for $R_{\rm P}/R_\star$ and the impact parameter, b. We see the well-known correlation between $R_{\rm P}/R_\star$ and b for large values of b. The Crossfield et al. (2016) analysis favored a grazing transit, and thus a larger value of $R_{\rm P}/R_\star$. Given the disagreement between the various reductions, we combined the three MCMC chains to derive a more conservative "adopted" value of $R_{\rm P}/R_\star$.

We obtained high-resolution speckle imaging at 692 nm with the Differential Speckle Survey Instrument (DSSI; Horch et al. 2012), a visitor instrument used at the Gemini-North 8.1 m telescope on 2016 January 13. The observations revealed no additional companions with $\Delta V < 2.5$ mag in the K2 photometric aperture down to separations of 80 mas, or ≈ 32 au in projected separation at the distance[19] of K2-108. Additional high-resolution imaging with DSSI at 880 nm and Keck/NIRC2 at the K-band also revealed no additional companions. Of the three high-resolution images, the DSSI image at 692 nm (shown in Figure 8) provides the tightest contrast curve in the *Kepler* bandpass. All imaging data sets are available on the Exoplanet Follow-up Observing Program (ExoFOP) website.[20]

A stellar companion having $a \approx 1$–40 au would have evaded the aforementioned follow-up observations. However, such an object would induce a reflex acceleration on K2-108, which would be easily detectable by our RVs:

$$\dot\gamma \approx \frac{GM_\star}{a^2} \approx 120 \text{ m s}^{-1}\text{ yr}^{-1}\left(\frac{M_\star}{M_\odot}\right)\left(\frac{a}{40 \text{ au}}\right)^{-2}.$$

Over the ~ 1 year observation baseline, we see only weak evidence for long-term acceleration ($\dot\gamma = -11.0 \pm 2.3$ m s^{-1} yr^{-1}). To be

---

[19] $d \approx 400$ pc computed according to the same technique used for K2-39 (see Section 3).
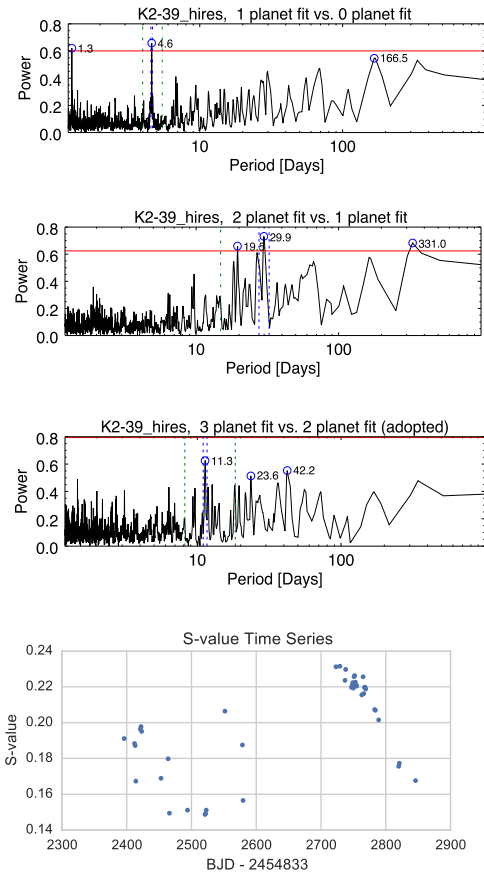[20] https://exofop.ipac.caltech.edu/k2/

Figure 4. Searches for Keplerian signals in the radial velocity (RV) time series of K2-39 (see Section 4.3). The top three panels show searches for Keplerian signatures in the HIRES RV time series of K2-39 using a Two-dimensional Keplerian Lomb–Scargle (2DKLS) periodogram. The bottom panel shows the S-values for K2-39, which traces stellar activity. First panel: the 2DKLS search of the HIRES data reveals a peak at $P = 4.6$ days, which corresponds to K2-39b, the transiting planet. Second panel: change in χ^2 when comparing a two-planet fit to a one-planet fit (power). There are several putative signals that are more significant than the 10% eFAP threshold plotted in red (Howard & Fulton 2016). However, the ≈ 330 day signal is associated with an activity cycle, seen in the S-values. We fit this activity signal with a Keplerian, and perform a final 2DKLS search for additional planets, shown in the third panel. All other potential signals fall below the 10% eFAP threshold.

consistent with the observed $\dot\gamma$, a companion at ≈ 40 au would be $\lesssim 0.1 M_\odot$ and much too faint to alter the derived planet radius. At smaller separations, the limits on the mass of a putative companion grow more stringent.

5. Discussion

5.1. Mass and Radius

Here, we put the four sub-Saturns presented in this paper in the context of other planets in their size class. Starting with the database of exoplanet properties hosted at the NASA Exoplanet Archive (NEA; Akeson et al. 2013), we constructed a list of sub-Saturns from the literature that have densities measured to 50% or better. We supplemented the list with additional measurements that have yet to be ingested into the NEA and removed a few planets with unreliable measurements. Including the measurements from this work, we found 19 sub-Saturns that passed our quality cuts; they are listed in Table 7.

In Figure 9, we show the measured masses and sizes of these planets, highlighting the measurements from this work.
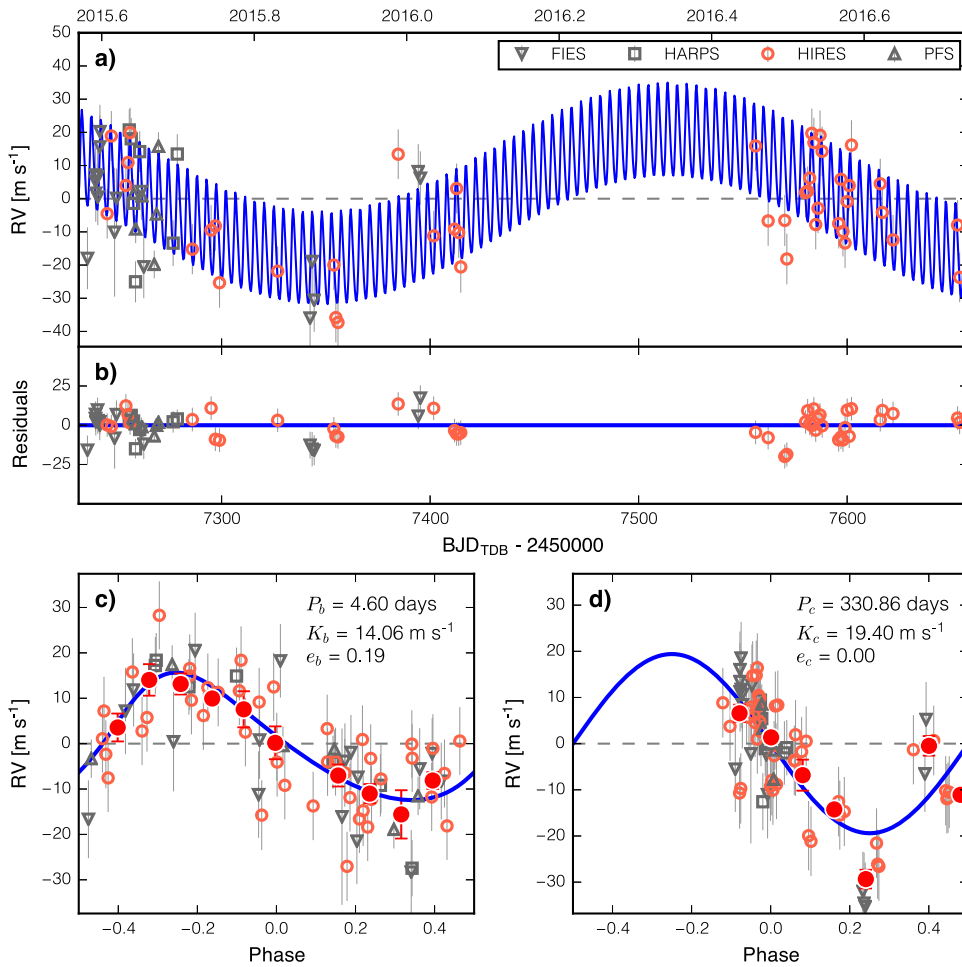
Figure 5. Fit to the K2-39 radial velocities (RVs) with two Keplerians (see Section 4.3). (a) Time series of RVs from HIRES along with FIES, HARPS, and PFS published in Van Eylen et al. (2016a). During the fitting we allowed for an arbitrary offset between the four instruments to float as a free parameter. The blue line shows the most probable two-Keplerian model. The long-period Keplerian models out a long-period activity cycle, which is also apparent in the S-values. (b) Residuals to the most probable Keplerian model. Panels (c) and (d) show the phase-folded RVs and the most probable Keplerian model with the contributions from the other planets removed. The large red circles show the phase-binned RVs. Note that because the posterior on e_b is asymmetric, the eccentricity of the most probable Keplerian differs slightly from the value reported in Table 5 ($e_b = 0.152^{+0.084}_{-0.068}$), which reflects the median of the posterior distribution.

Remarkably, for sub-Saturns, there is little correlation between a planet's mass and size. These planets have a nearly uniform distribution of mass from $M_P \approx 6$–$60 \, M_\oplus$. We note that the hottest planets tend to have higher masses, while cool planets have both high and low masses. Figure 10 shows planet mass and radius, cast in terms of planet size and planet density. The decreasing densities toward larger sizes can be understood simply in terms of larger radii, given there is no strong trend of larger planet masses with larger planet size.

5.2. Planetary Envelope Fraction

One advantage of sub-Saturns is that in this size range, both heavy elements and low-density gaseous envelopes contribute significantly to the total planet mass. A consequence is, to first order, sub-Saturns can be approximated as two-component planets consisting of a rocky heavy-element core, surrounded by an envelope of H/He (Lopez & Fortney 2014; Petigura et al. 2016). Here we use the results of Lopez & Fortney (2014), who simulated the internal structure and thermal evolution of planets with solar-composition H/He envelopes atop Earth-composition cores. These simulations were run over a wide swath of parameter space for planets with different masses, M_P, different envelope fractions, $f_{env} = M_{env}/M_P$, and on orbits receiving different levels of incident stellar irradiation, S_{inc}. The model planets were allowed to evolve over time and Lopez & Fortney (2014) noted the planet radii at specified intervals. The result of these simulations is a four-dimensional grid of planet radius, R_P, sampled at various combinations of (M_P, f_{env}, S_{inc}, age).

We used this grid to solve for the values of the planet f_{env} that are consistent with the observed (M_P, R_P, S_{inc}, and age). We drew M_P, R_P, and S_{inc} measured posterior distributions and interpolated the model grid in order to derive f_{env}. We assumed a uniform age of 5 Gyr. With the exception of a few stars analyzed with asteroseismology, most of the system ages are derived from isochrone fitting and are thus uncertain at the ≈ 2–3 Gyr level. Fortunately, the derived f_{env} fraction is not sensitive to the adopted system age. Adopting a uniform age of 2 Gyr resulted in a typical change in the derived f_{env} of $\approx 2\%$. The resulting values of f_{env} are listed in Table 7.

We have made several approximations when computing f_{env}. We have ignored the possibility of water or other volatile ices contributing significantly to the heavy-element cores of

Table 5
K2-39 Planet Parameters

	Value		Reference
Stellar Parameters			
Identifiers	EPIC-206247743		
	TYC-5811-835-1		
$T_{\rm eff}$ (K)	4912 ± 60		A
$\log g$ (dex)	3.58 ± 0.05		A
[Fe/H] (dex)	0.43 ± 0.04		A
$v \sin i$ (km s^{-1})	0.1		A
$M_\star$ ($M_\odot$)	$1.192^{+0.085}_{-0.070}$		A
$R_\star$ ($R_\odot$)	2.93 ± 0.21		A
Age (Gyr)	$6.7^{+1.7}_{-1.3}$		A
Apparent V (mag)	10.83 ± 0.08		A
Transit Model			
P (days)	4.60497 ± 0.00077		B
T_0 (BJD-2454833)	2152.4315 ± 0.0058		B
$R_{\rm P}/R_\star$ (%)	1.79 ± 0.13		A
$R_{\rm P}$ ($R_\oplus$)	5.71 ± 0.63		A
a (au)	0.0574 ± 0.0012		A
$S_{\rm inc}$ ($S_\oplus$)	1356 ± 175		A
$T_{\rm eq}$ (K)	1670 ± 54		A
Circular RV Model			
P (days)	fixed	329 ± 10	B
T_0(BJD)	fixed	2456940 ± 16	B
K (m s^{-1})	12.7 ± 1.3	17.4 ± 2.8	A
$\gamma_{\rm HIRES}$ (m s^{-1})	2.1 ± 2.2		A
$\gamma_{\rm HARPS}$ (m s^{-1})	-3.4 ± 3.9		A
$\gamma_{\rm PFS}$ (m s^{-1})	1.3 ± 3.6		A
$\gamma_{\rm FIES}$ (m s^{-1})	2.7 ± 3.1		A
$\dot{\gamma}$ (m s^{-1} yr^{-1})	0 (fixed)		A
$\sigma_{\rm jit,HIRES}$ (m s^{-1})	7.42 ± 0.86		A
$\sigma_{\rm jit,HARPS}$ (m s^{-1})	6.7 ± 1.4		A
$\sigma_{\rm jit,PFS}$ (m s^{-1})	5.8 ± 1.4		A
$\sigma_{\rm jit,FIES}$ (m s^{-1})	7.2 ± 1.6		A
$M_{\rm P}$ ($M_\oplus$)	37.3 ± 4.3	$\cdots$	A
ρ(g cm^{-3})	$1.10^{+0.44}_{-0.31}$	$\cdots$	A
Eccentric RV Model (Adopted)			
P (days)	fixed	327.2 ± 9.8	B
T_0 (BJD)	fixed	2456614 ± 25	B
K (m s^{-1})	13.8 ± 1.4	18.4 ± 2.9	A
e	$0.152^{+0.084}_{-0.068}$	$\cdots$	A
$\gamma_{\rm HIRES}$ (m s^{-1})	1.9 ± 2.2		A
$\gamma_{\rm HARPS}$ (m s^{-1})	24486.6 ± 3.9		A
$\gamma_{\rm PFS}$ (m s^{-1})	-1.7 ± 3.5		A
$\gamma_{\rm FIES}$ (m s^{-1})	24574.5 ± 3.0		A
$\dot{\gamma}$ (m s^{-1} yr^{-1})	0 (fixed)		A
$\sigma_{\rm jit,HIRES}$ (m s^{-1})	7.57 ± 0.86		A
$\sigma_{\rm jit,HARPS}$ (m s^{-1})	6.3 ± 1.4		A
$\sigma_{\rm jit,PFS}$ (m s^{-1})	5.0 ± 1.5		A
$\sigma_{\rm jit,FIES}$ (m s^{-1})	6.7 ± 1.6		A
$M_{\rm P}$ ($M_\oplus$)	39.8 ± 4.4	$\cdots$	A
ρ (g cm^{-3})	$1.17^{+0.47}_{-0.32}$	$\cdots$	A

Note. A: this work; B: Crossfield et al. (2016). We model a large amplitude ($\approx$20 m s^{-1}) stellar activity signal by introducing an additional circular Keplerian.

these planets. Lopez & Fortney (2014), however, showed that including ices in the core does not significantly alter the radius–composition relationship for planets in this size range. Because the H/He envelope represents most of the planet volume, our inferred $f_{\rm env}$ does not depend sensitively on the detailed composition of the planet core. We have also assumed that all the heavy elements are concentrated in the planets' cores rather than being distributed throughout the envelope.

5.3. Role of Photo-evaporation Among Sub-Saturns

If photo-evaporation plays a dominant role in sculpting the gaseous envelopes of sub-Saturns, one might expect the envelope fraction, $f_{\rm env}$, to correlate with the energy it receives from its host star. Figure 11 shows the total planet mass ($M_{\rm P}$) and envelope fraction ($f_{\rm env}$) as a function of the blackbody equilibrium temperature. As a matter of convenience, we include core mass ($M_{\rm core}$) and envelope mass ($M_{\rm env}$), which can be trivially computed from $M_{\rm P}$ and $f_{\rm env}$. We do not observe a strong one-to-one correlation envelope fraction and equilibrium temperature. We do, however, observe that cool planets span a large range of $f_{\rm env} \approx 10\%$–50% while hot planets span a more narrow range of $f_{\rm env} \approx 10\%$–20%. Perhaps photo-evaporation excludes planets from occupying certain domains in the $f_{\rm env}$–$T_{\rm eq}$ plane.

To further explore the possible role of photo-evaporation, we considered two quantities that are more directly related to a planet's susceptibility to photo-evaporation: XUV heating and planet binding energy. XUV heating is the total lifetime-integrated XUV flux incident at a planet's orbit multiplied by the planet's current cross section. Figure 12, which is updated from Lopez & Fortney (2014), shows the planet XUV heating (in ergs) versus planet binding energy (in erg). This sort of diagram has been used as supporting evidence for the role of photo-evaporation in sculpting the envelopes of highly irradiated sub-Neptunes (Lecavelier Des Etangs 2007; Lopez et al. 2012; Owen & Wu 2013). The dashed line shows the envelope survival threshold predicted by photo-evaporation and thermal evolution models in Lopez et al. (2012), and the absence of planets with gaseous envelopes above this line suggests that planets near this threshold have experienced photo-evaporation. Although a few sub-Saturns lie close to this threshold, most lie well below it, indicating that they are sufficiently massive or are on wide enough orbits to be immune to significant photo-evaporation.

5.4. Stellar Metallicity and Planet Metallicity

One may interpret present-day stellar metallicity as a proxy for the metal enrichment of the protoplanetary disk because the disk and star formed from the same molecular cloud. However, the mean metallicity of the protoplanetary disk may be different from the local disk metallicity at the location of planet formation. With this caveat in mind, we nonetheless looked for correlations between host star metallicity and the observed properties of sub-Saturns.

In contrast to equilibrium temperatures, we observe a stronger set of correlations between the planetary properties of sub-Saturns and host star metallicity, [Fe/H]. Figure 13 shows $M_{\rm P}$, $f_{\rm env}$, $M_{\rm core}$, and $M_{\rm env}$ against [Fe/H]. Sub-Saturns orbiting metal-rich stars tend to be more massive. Interestingly, both the planetary core mass, $M_{\rm core}$, and envelope mass, $M_{\rm env}$, appear to increase with stellar metallicity. This is understandable, however, given that planets with more massive cores should generally be able to accrete larger gaseous envelopes before their disks dissipate (Lee & Chiang 2015). This suggests that the metal-rich hosts had more solids available in their disk,
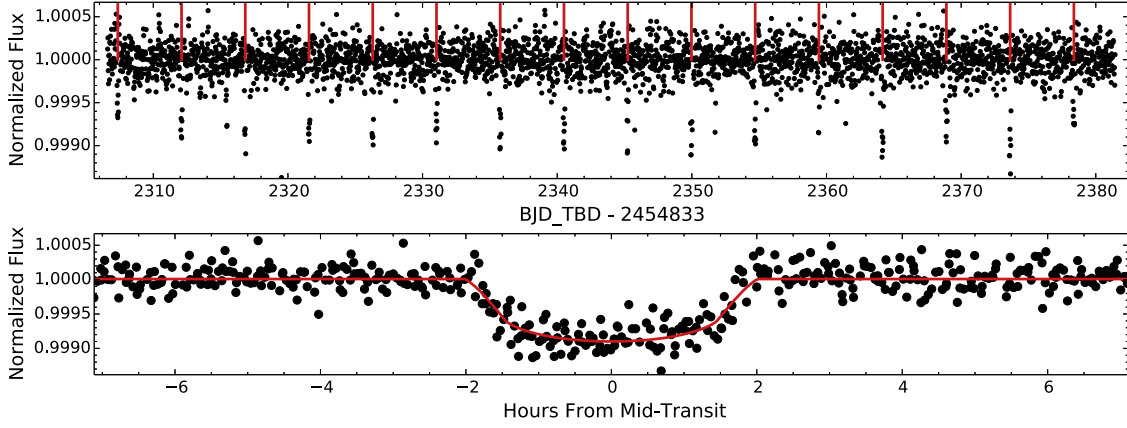
Figure 6. Top: *K2* light curve of K2-108 showing with the transits of K2-108b labeled with red ticks. Bottom: photometry phase-folded on the transit ephemeris.

Table 6
System Parameters of K2-108

	Value	Reference
Stellar Parameters		
Identifier	EPIC-211736671	
$T_{\rm eff}$ (K)	5474 ± 60	A
$\log g$ (dex)	3.99 ± 0.05	A
[Fe/H] (dex)	0.33 ± 0.04	A
$v \sin i$ (km s^{-1})	<2	A
$M_\star$ ($M_\odot$)	$1.121^{+0.065}_{-0.053}$	A
$R_\star$ ($R_\odot$)	1.75 ± 0.14	A
age (Gyr)	7.8 ± 1.5	A
Apparent V (mag)	12.33 ± 0.01	A
	Planet b	
Transit Model		
P (days)	4.73401 ± 0.00024	A
T_0 (BJD-2454833)	2312.0965 ± 0.0019	A
$R_{\rm P}$ ($R_\oplus$)	5.28 ± 0.54	A
a (au)	0.0573 ± 0.0010	A
$S_{\rm inc}$ ($S_\oplus$)	762 ± 100	A
$T_{\rm eq}$ (K)	1446 ± 48	A
Circular RV Model		
K (m s^{-1})	19.4 ± 2.3	A
$\gamma_{\rm HIRES}$ (m s^{-1})	-4.0 ± 1.6	A
$\dot{\gamma}$ (m s^{-1} yr^{-1})	0 (fixed)	A
$\sigma_{\rm jit,HIRES}$ (m s^{-1})	$6.0^{+1.5}_{-1.1}$	A
$M_{\rm P}$ ($M_\oplus$)	55.1 ± 6.8	A
ρ (g cm^{-3})	$2.05^{+0.75}_{-0.54}$	A
Eccentric RV Model (Adopted)		
K (m s^{-1})	21.3 ± 1.4	A
e	0.180 ± 0.042	A
$\gamma_{\rm HIRES}$ (m s^{-1})	-2.63 ± 0.91	A
$\dot{\gamma}$ (m s^{-1} yr^{-1})	-11.0 ± 2.3	A
$\sigma_{\rm jit,HIRES}$ (m s^{-1})	$2.86^{+1.01}_{-0.78}$	A
$M_{\rm P}$ ($M_\oplus$)	59.4 ± 4.4	A
ρ (g cm^{-3})	$2.22^{+0.77}_{-0.55}$	A

Note. A: this work.

allowing those sub-Saturns to form more massive cores, and that these larger cores were then able accrete more massive envelopes.

It is worthwhile to compare the observed $M_{\rm P}$–[Fe/H] trend to the stellar metallicity distribution of *Kepler* planet hosts. Buchhave et al. (2012) observed that planets smaller than $\approx 4\ R_\oplus$

are found around stars of wide-ranging metallicities ($-0.5 \lesssim$ [Fe/H] $\lesssim +0.5$ dex), while larger planets are typically found around more metal-rich stars ($-0.2 \lesssim$ [Fe/H] $\lesssim +0.5$ dex). This is consistent with our sample, constructed from planets found by *Kepler*, *K2*, and other surveys. Stellar metallicity of > -0.2 dex seems to be an important criterion for forming sub-Saturns. However, the additional metals in the disk seem to result in more massive final planets.

The path through which increased metallicity produces more massive sub-Saturns could proceed in one of two ways: (1) disks with more solid material form substantially more massive planet cores that grow smoothly into more massive planets or (2) disks with more solid material form slightly more massive cores that perturb neighboring planets causing collisions and mergers. We have a slight preference for the latter explanation, given the eccentricity distribution of sub-Saturns, explored in Section 5.5. It is also plausible that metal-enriched disks could form planet cores more quickly, allowing for a long period of gas accretion. However, we see no evidence of this given the absence of a strong correlation between $f_{\rm env}$ and host star metallicity.

In addition to the trends with stellar metallicity shown in Figure 13, it is also interesting to examine whether there are trends in the heavy-element abundances of sub-Saturns after controlling for the dependence on stellar metallicity. Recently, Thorngren et al. (2016) examined planet metal mass fraction, $Z_{\rm P}$, for 47 planets having $M_{\rm P} \approx 30$–$3000\ M_\oplus$ relative to the heavy-element fraction of their parent stars, $Z_\star = Z_\odot 10^{\rm [Fe/H]}$. $Z_{\rm P}$ was computed via $Z_{\rm P} = M_{\rm core}/M_{\rm env}$ using thermal evolution models similar to those used here. Thorngren et al. (2016) observed an anti-correlation between $M_{\rm P}$ and $Z_{\rm P}/Z_\star$. They argued that such an anti-correlation can be understood in terms of traditional core-accretion formation theory if one assumes that planets below the isolation mass are able to accrete all of the solids in their isolation zone, typically ≈ 3.5 Hill radii (Lissauer 1993), but not all of their gas. Given these assumptions, Equation (9) of Thorngren et al. (2016) predicts the planetary metal enrichment:

$$\frac{Z_{\rm P}}{Z_\star} = 3 f_H f_e \frac{H}{a} Q^{-1} \left(\frac{M_{\rm P}}{M_\star} \right)^{-2/3}. \qquad (1)$$

Here, $f_H \sim 3.5$ is the approximate number of Hill radii from which a planet can effectively accrete solids, $f_e \sim 1$ is an enrichment factor to allow for metal enhancement due to radial drift by solids, H is the disk scale height, a is the semimajor axis, and Q is the Toomre disk instability parameter (Toomre
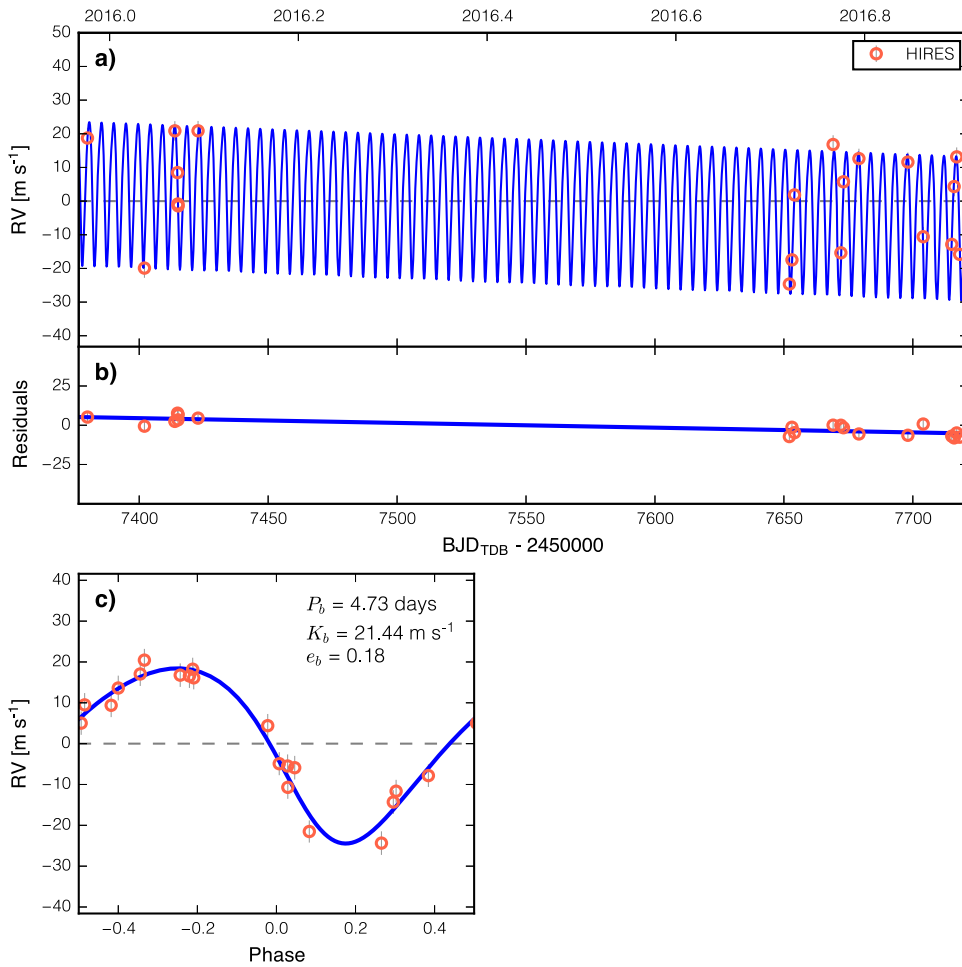
Figure 7. Single Keplerian model fit to the K2-108 radial velocities (RVs), allowing for eccentricity (see Section 4.4). (a) Time series of RVs from HIRES. The blue line shows the most probable Keplerian model. (b) Residuals to the most probable Keplerian model. (c) The phase-folded RVs and the most probable Keplerian model.
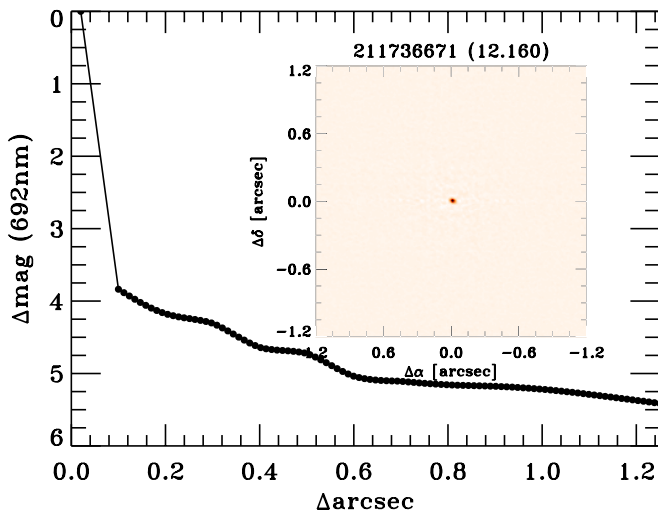

Figure 8. Contrast curve of K2-108 (EPIC-211736671) taken with a narrow-band filter centered at 692 nm using the DSSI camera (Horch et al. 2012) on the Gemini-N 8 m telescope. The inset image shows the 2 × 2 arcsec region centered on K2-108 reconstructed from the speckle image sequence. Putative companions with contrasts of <2.5 mag, which could alter the inferred planet size, are ruled out for separations >80 mas. Additional DSSI observations at 880 nm and Keck/NIRC2 observations at the K-band also reveal no additional companions to K2-108. See Section 4.4 for further details.

1964). Thorngren et al. (2016) found that Equation (1) can reproduce the observed trend between M_P and $Z_P/Z_\star$ if $f_H = 3.5$, $f_e = 1$, and $Q = 5$.

Figure 14 compares our sample of sub-Saturns to the predictions of Equation (1). Sub-Saturns are a valuable laboratory for testing the physics of envelope accretion because they are larger than the sub-Neptunes, which typically have $f_{env} \lesssim 10\%$, and the gas giants, which are nearly entirely envelope ($f_{env} \sim 100\%$). Following Thorngren et al. (2016), we approximate the planetary metal abundance by setting $Z_P = M_{core}/M_P$. For the most massive sub-Saturns (having $M_P/M_\star \gtrsim 10^{-4}$), where our sample overlaps with the Thorngren et al. (2016) sample, we find good agreement with the predictions of Equation (1), as shown by the dotted line. Below $M_P/M_\star \sim 10^{-4}$, however, we find a significant increase in dispersion below this relation, with many planets being significantly less enriched in metals than expected from Equation (1).

One interpretation is that this increase in scatter simply reflects the natural transition between giant planets, which essentially accrete all of the heavy elements in their feeding zones, and low mass planets, which do not. Equation (1) assumes that the solids in the disk have fully decoupled from the gas, and that a planet can successfully accrete all of the

Table 7
Sub-Saturns with Well-measured Densities

Name	N_P	R_P $R_\oplus$	M_P $M_\oplus$	ρ g cm^{-3}	e	T_{eq} K	f_{env} %	[Fe/H] dex
Kepler-4 b	1	$4.00^{+0.21}_{-0.21}$	$24.5^{+3.8}_{-3.8}$	$2.09^{+0.53}_{-0.44}$	...	1597	$6.7^{+1.3}_{-1.4}$	+0.17
GJ 436b	1	$4.17^{+0.17}_{-0.17}$	$22.1^{+2.3}_{-2.3}$	$1.67^{+0.30}_{-0.26}$	$0.1383^{+0.0002}_{-0.0002}$	659	$12.6^{+1.9}_{-1.9}$	...
Kepler-11 e	6	$4.19^{+0.07}_{-0.09}$	$8.0^{+1.5}_{-2.1}$	$0.60^{+0.15}_{-0.14}$	$0.0120^{+0.0060}_{-0.0060}$	630	$14.9^{+0.7}_{-0.7}$	−0.04
Kepler-413 b	1	$4.35^{+0.10}_{-0.10}$	$51.0^{+22.0}_{-21.0}$	$2.40^{+1.00}_{-1.00}$	$0.1185^{+0.0018}_{-0.0017}$	348	$10.8^{+3.8}_{-2.0}$	...
K2-27b	1	$4.48^{+0.23}_{-0.23}$	$30.9^{+4.6}_{-4.6}$	$1.88^{+0.46}_{-0.38}$	$0.2510^{+0.0880}_{-0.0880}$	910	$13.9^{+2.4}_{-2.5}$	+0.13
Kepler-223 e	4	$4.60^{+0.27}_{-0.41}$	$4.8^{+1.4}_{-1.2}$	$0.27^{+0.11}_{-0.09}$	$0.0510^{+0.0190}_{-0.0190}$	944	$16.5^{+2.5}_{-2.6}$	+0.06
HAT-P-11 b	1	$4.73^{+0.16}_{-0.16}$	$25.7^{+2.9}_{-2.9}$	$1.34^{+0.22}_{-0.20}$	$0.1980^{+0.0460}_{-0.0460}$	861	$17.1^{+1.5}_{-1.5}$	+0.31
K2-32b	3	$5.13^{+0.28}_{-0.28}$	$16.5^{+2.7}_{-2.7}$	$0.67^{+0.18}_{-0.15}$	...	815	$22.5^{+3.0}_{-3.1}$	−0.02
Kepler-25 c	3	$5.20^{+0.09}_{-0.09}$	$24.6^{+5.7}_{-5.7}$	$0.96^{+0.24}_{-0.23}$	...	1018	$21.4^{+1.3}_{-1.3}$	−0.04
Kepler-223 d	4	$5.24^{+0.26}_{-0.45}$	$8.0^{+1.5}_{-1.3}$	$0.30^{+0.10}_{-0.07}$	$0.0370^{+0.0180}_{-0.0170}$	1040	$22.3^{+3.4}_{-3.2}$	+0.06
K2-108b	1	$5.28^{+0.54}_{-0.54}$	$59.4^{+4.4}_{-4.4}$	$2.21^{+0.90}_{-0.59}$	$0.1800^{+0.0420}_{-0.0420}$	1440	$16.0^{+4.8}_{-5.4}$	+0.33
Kepler-18 c	3	$5.49^{+0.26}_{-0.26}$	$17.3^{+1.9}_{-1.9}$	$0.57^{+0.12}_{-0.10}$	...	979	$25.7^{+2.6}_{-2.8}$	+0.19
K2-24 b	2	$5.68^{+0.56}_{-0.56}$	$21.0^{+5.4}_{-5.4}$	$0.62^{+0.31}_{-0.22}$	...	766	$28.4^{+7.4}_{-6.2}$	+0.42
K2-39b	1	$5.71^{+0.63}_{-0.63}$	$39.7^{+4.6}_{-4.6}$	$1.16^{+0.54}_{-0.34}$	$0.1500^{+0.0760}_{-0.0760}$	1689	$18.1^{+5.2}_{-4.8}$	+0.43
Kepler-101 b	2	$5.77^{+0.85}_{-0.79}$	$51.1^{+5.1}_{-4.7}$	$1.46^{+0.90}_{-0.50}$	$0.0860^{+0.0800}_{-0.0590}$	1547	$19.5^{+7.9}_{-6.9}$	+0.33
Kepler-87 c	2	$6.14^{+0.29}_{-0.29}$	$6.4^{+0.8}_{-0.8}$	$0.15^{+0.03}_{-0.03}$	$0.0390^{+0.0120}_{-0.0120}$	440	$35.6^{+3.4}_{-3.7}$	−0.17
HATS-7 b	1	$6.31^{+0.52}_{-0.38}$	$38.1^{+3.8}_{-3.8}$	$0.83^{+0.23}_{-0.17}$	...	1070	$33.3^{+6.1}_{-5.8}$	+0.25
HAT-P-26 b	1	$6.33^{+0.81}_{-0.36}$	$18.8^{+2.2}_{-2.2}$	$0.40^{+0.15}_{-0.10}$	$0.1240^{+0.0600}_{-0.0600}$	981	$35.8^{+6.9}_{-7.5}$	−0.04
CoRoT-8 b	1	$6.39^{+0.22}_{-0.22}$	$69.9^{+9.5}_{-9.5}$	$1.47^{+0.27}_{-0.25}$	...	844	$32.2^{+3.5}_{-3.1}$	+0.30
Kepler-56 b	3	$6.51^{+0.29}_{-0.28}$	$22.1^{+3.9}_{-3.6}$	$0.44^{+0.10}_{-0.09}$	...	1479	$26.3^{+2.4}_{-2.4}$	+0.37
Kepler-18 d	3	$6.98^{+0.33}_{-0.33}$	$16.4^{+1.4}_{-1.4}$	$0.26^{+0.05}_{-0.04}$	...	784	$44.5^{+3.2}_{-3.6}$	+0.19
Kepler-79d	4	$7.16^{+0.13}_{-0.16}$	$6.0^{+2.1}_{-1.6}$	$0.09^{+0.03}_{-0.03}$	$0.0250^{+0.0590}_{-0.0230}$	626	$42.6^{+2.5}_{-3.3}$	−0.02
K2-24 c	2	$7.82^{+0.72}_{-0.72}$	$27.0^{+6.9}_{-6.9}$	$0.31^{+0.14}_{-0.10}$	...	605	$57.3^{+9.1}_{-9.9}$	+0.42

Note. List of sub-Saturns having densities measured to 50% or better, assembled from the NASA Exoplanet Archive, this work, and other sources. N_P—total number of detected planets in the system, e—orbital eccentricity; we do not report eccentricity if only upper limits are available. T_{eq} refers to the blackbody temperature (i.e., assuming zero albedo). f_{env}—"envelope fraction," i.e., fraction of planet's mass in H/He in the two-component modeling of planet mass and radius, described in Section 5.2. Notes on individual systems: Kepler-4 b—Borucki et al. (2010b), GJ 436b—Butler et al. (2004), Kepler-11 e—Lissauer et al. (2013), Kepler-413 b—Kostov et al. (2014), K2-27b —This work, Kepler-223 e—Mills et al. (2016), HAT-P-11 b—Bakos et al. (2010), K2-32b—This work, Kepler-25 c—Marcy et al. (2014), Kepler-223 d—Mills et al. (2016), K2-108b—This work, Kepler-18 c—Cochran et al. (2011), K2-24 b—Petigura et al. (2016), K2-39b—This work, Kepler-101 b—Bonomo et al. (2014), Kepler-87 c—Ofir et al. (2014), HATS-7 b—Bakos et al. (2015), HAT-P-26 b—Hartman et al. (2011), CoRoT-8 b—Bordé et al. (2010), adopted 3 ± 1 Gyr; Kepler-56 b—Huber et al. (2013), Kepler-18 d—Cochran et al. (2011), Kepler-79d—Jontof-Hutter et al. (2014), K2-24 c—Petigura et al. (2016).

solids near its isolation zone. At lower core masses, gravitational focusing becomes more important, gas damping of planetesimals eccentricities becomes more efficient, and collision and growth timescales become longer. All of these factors mean less massive cores may not accrete all solids within ≈3.5 Hill radii, which may instead be dispersed or incorporated into other planets in compact, multiplanet systems. In summary, we examined whether the correlation between planet metal enrichment and planet masses observed by Thorngren et al. (2016) for planets having $M_P = 30$–$3000 \, M_\oplus$ is present among the sub-Saturns. We do not observe a strong correlation, indicating a possible transition in the formation pathways of planets with $M_P \lesssim 30 \, M_\oplus$.

5.5. Eccentricity and Planet Multiplicity

The fits to K2-27, K2-39, and K2-108 RVs favored non-zero orbital eccentricities of 0.251 ± 0.088, $0.152^{+0.084}_{-0.068}$, and 0.180 ± 0.042, respectively. Given that these planets are on short orbital periods of 4.6–6.8 days, respectively, it is worthwhile to consider the extent to which tides are expected to damp away eccentricity. The timescale for eccentricity damping (Goldreich & Soter 1966) is given by

$$\tau_e = \frac{4}{63}\left(\frac{Q'}{n}\right)\left(\frac{M_P}{M_\star}\right)\left(\frac{a}{R_P}\right)^5. \quad (2)$$

Here, $n = \sqrt{GM_\star/a^3}$ is the mean motion, and Q', the modified tidal quality factor, is given by $Q' = 3Q/2k_2$, where Q is the specific dissipation function and k_2 is the Love number (see Goldreich & Soter 1966; Murray & Dermott 1999; Mardling & Lin 2004). Q' is quite uncertain even for planets in the solar system. As a point of reference Lainey et al. (2017) give $Q' \approx$ 6000–18,000 for Saturn, based on *Cassini* ranging data. Tittemore & Wisdom (1989, 1990) give $Q \approx$ 11,000–39,000 for Uranus based on studies of the Uranian satellites, which translates to $Q' \approx$ 165,000–585,000, adopting $k_2 = 0.104$ from Gavrilov & Zharkov (1977). Q' is even more uncertain for sub-Saturns, which have no solar system analogues. Here, we adopt $Q' = 10^5$ for the sub-Saturns, with the understanding that this estimate is only good to an order of magnitude. Re-writing
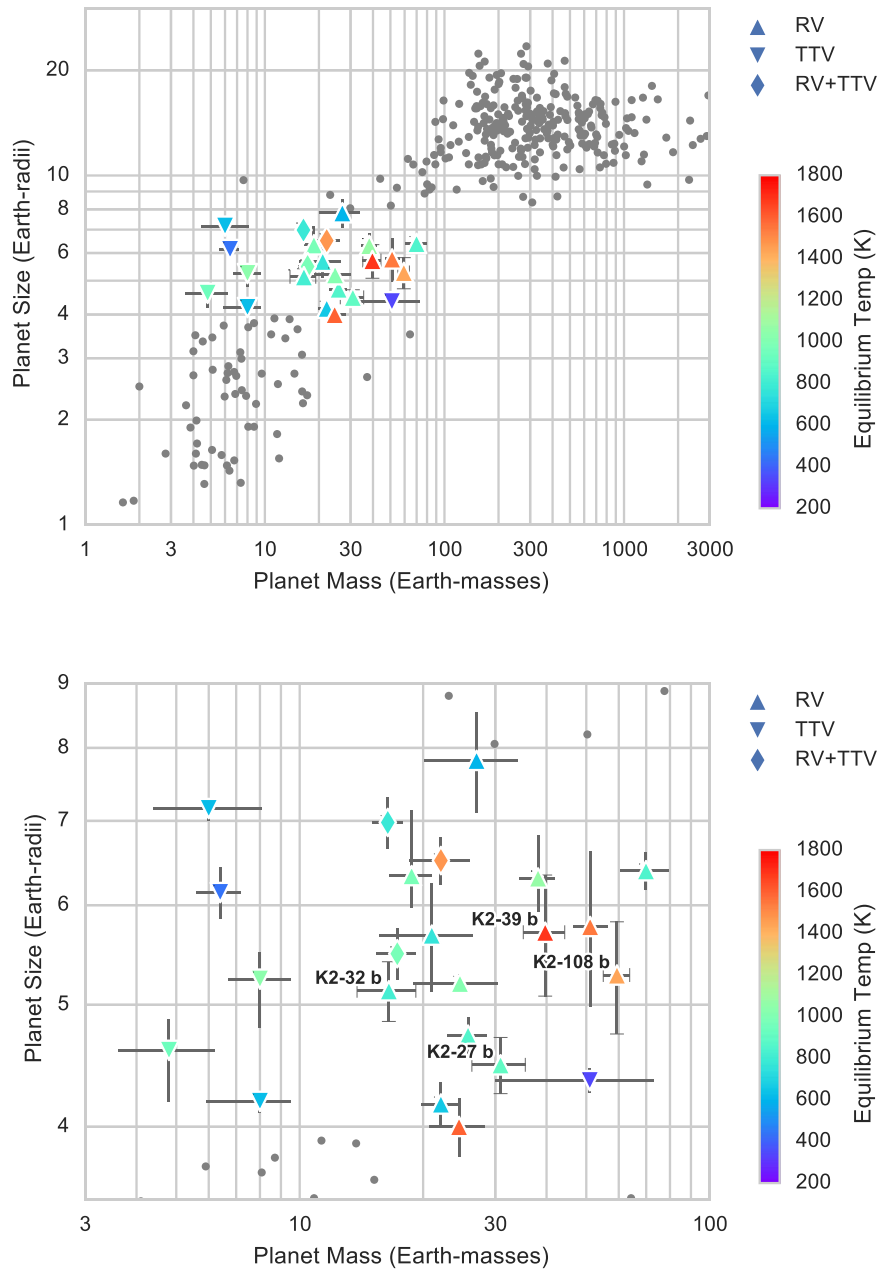
Figure 9. Top: masses and radii of sub-Saturns having densities measured to 50% or better. Planets of different size classes with comparable density precision are shown as gray points for context. For the sub-Saturns, symbol colors correspond to the blackbody equilibrium temperature. The symbol shapes correspond to the method by which planet masses were measured: radial velocities (RVs), transit-timing variations (TTVs), or a combined analysis (RVs+TTVs). For sub-Saturns, we note almost no correlation between planet mass and planet size. Bottom: a zoomed-in view of the top panel, focusing on sub-Saturns. See Section 5.1 for additional details.

Equation (2),

$$\tau_e \sim 1.8 \, \text{Gyr} \left(\frac{Q'}{10^5} \right) \left(\frac{P}{10 \, \text{days}} \right) \left(\frac{M_P}{10 \, M_\oplus} \right) \left(\frac{M_\star}{M_\odot} \right)^{-1}$$
$$\times \left(\frac{a}{0.05 \, \text{au}} \right)^5 \left(\frac{R_P}{4 \, R_\oplus} \right)^{-5}.$$

For K2-27b, we find $\tau_e \sim 10 \, \text{Gyr}$, comparable to the age of the system, suggesting that if this eccentricity was caused by planet–planet scattering early in the star's lifetime, the eccentricity could persist to the present day. K2-39b and K2-108b are slightly larger than K2-27b and also orbit closer to their host stars. Because the circularization timescale is a strong function of a/R_P, they have substantially shorter τ_e of $\sim 0.6 \, \text{Gyr}$ and $\sim 2 \, \text{Gyr}$, respectively. These circularization timescales are formally shorter than the age of their host stars and present some challenges for understanding any present day eccentricities. This tension could be resolved if Q' is $\sim 10^6$ as opposed to the assumed value of $\sim 10^5$. Eccentric orbits could also be maintained by additional yet undetected planets. Deming et al. (2007) proposed such an explanation for GJ 436b, another short-period eccentric sub-Saturn (see Table 7). Assuming $Q' \sim 10^5$, τ_e for GJ 436b is only $\sim 0.1 \, \text{Gyr}$. Although no additional planets have been detected in the GJ 436 system, Batygin et al. (2009) showed this explanation to be plausible in the context of secular theory.
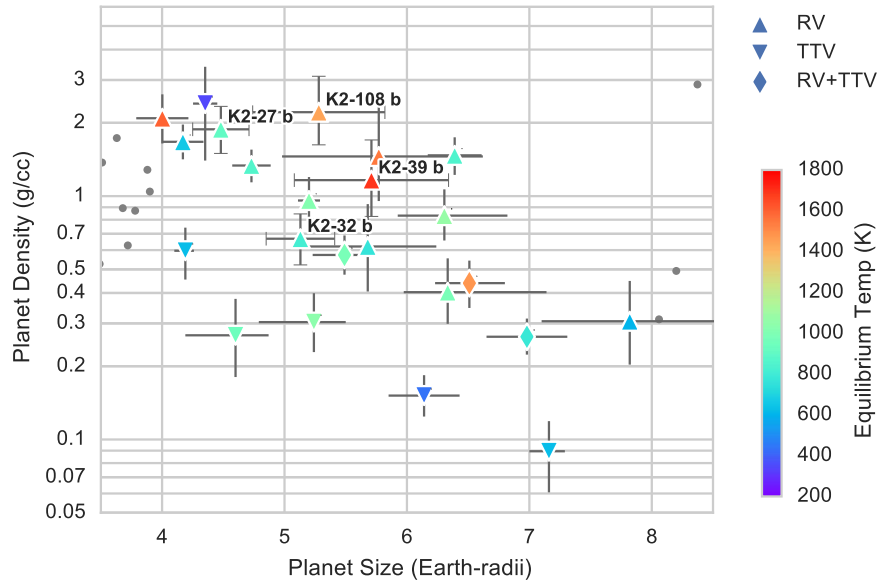
Figure 10. Same as Figure 9 but showing mean planet density as a function of planet size. For planets of a given size, there is a diversity of densities due to the diversity in planet mass. Although the hottest planets seem to have high densities for their size, cool planets span a wide range of density.
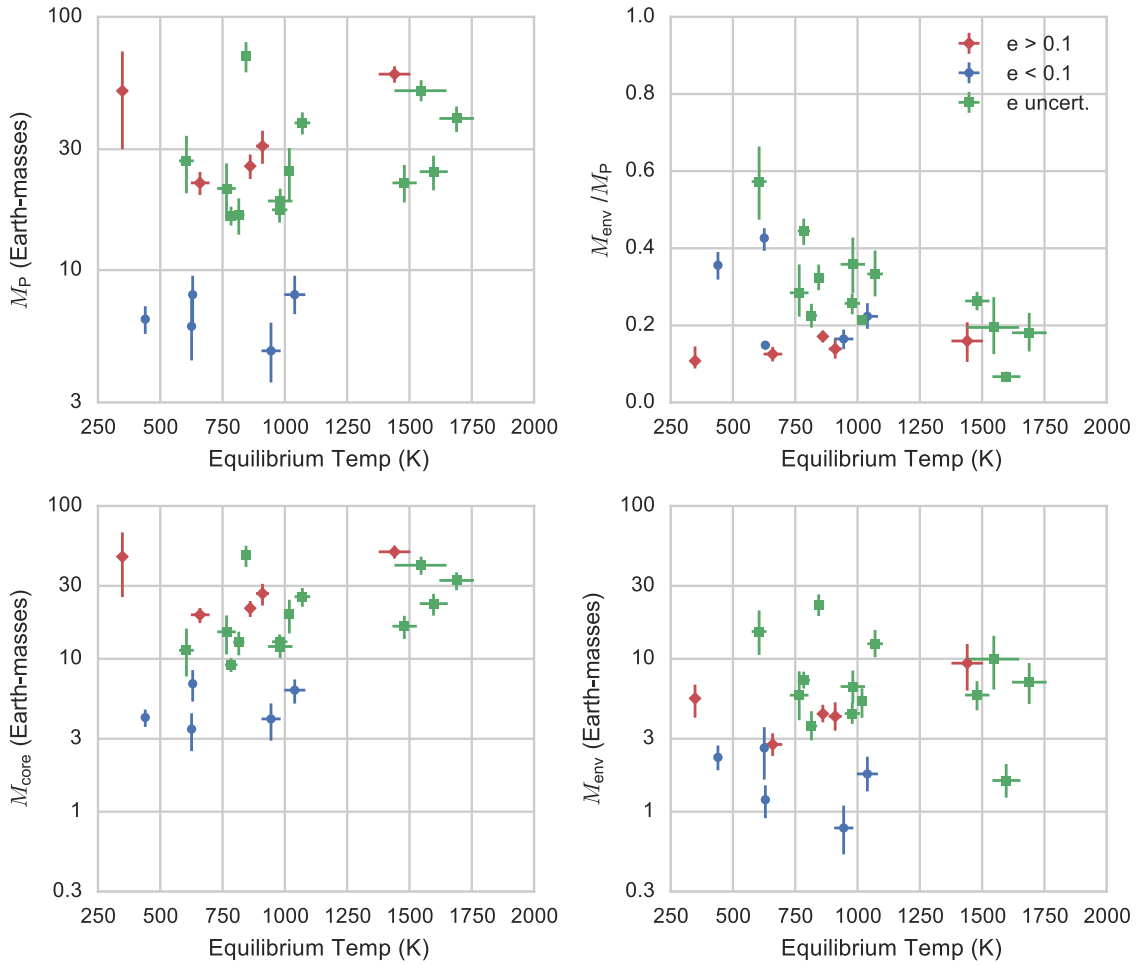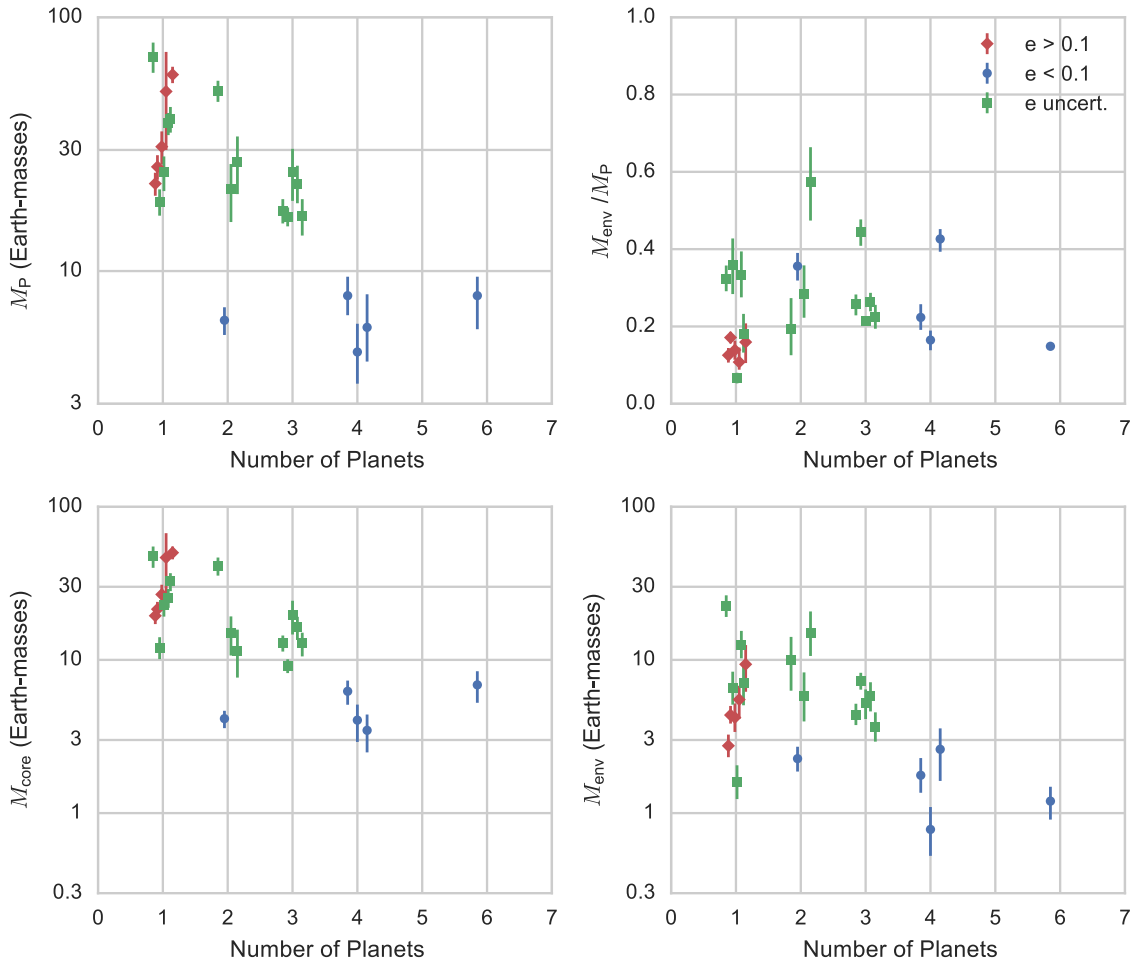

Figure 11. Panels (a)–(d) show the planet mass (M_P), envelope fraction (M_{env}/M_P), core mass (M_{core}), and envelope mass (M_{env}) as a function of planet blackbody equilibrium temperature (T_{eq}). We observe an absence of planets having high envelope fractions ($f_{env} \gtrsim 0.25$) at high equilibrium temperatures as expected from photo-evaporation. However, the lack of a strong trend between T_{eq} and f_{env} suggests that photo-evaporation has not significantly sculpted the majority of sub-Saturns shown. Planets where eccentricity has been constrained to be less than or greater than 0.1 are colored blue and red, respectively.
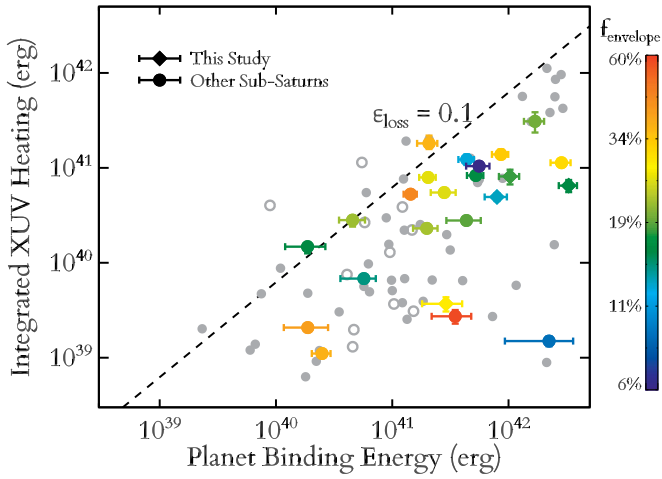
Figure 12. Total lifetime XUV heating planets receive at their orbit vs. their current binding energy. Sub-Saturns are color-coded by their current gaseous envelope fraction, while all other planets $<100\,M_\oplus$ are shown in gray. The dashed line meanwhile shows the predicted photo-evaporation threshold from Lopez et al. (2012). This indicates that only a few of the sub-Saturns in this sample have likely been strongly affected by photo-evaporation.
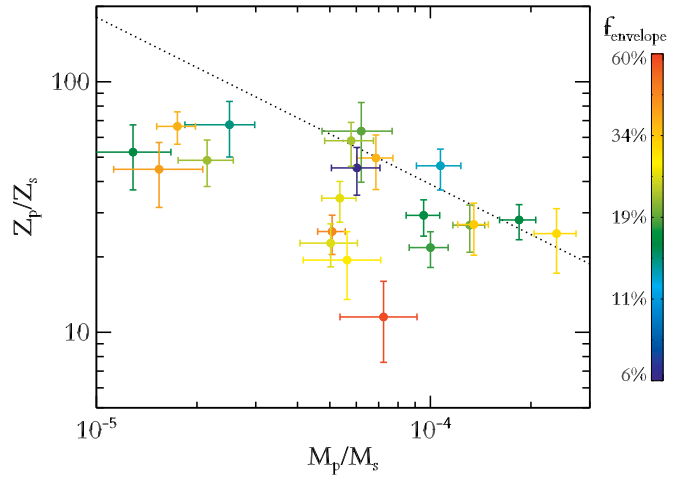
Figure 14. Bulk heavy-element enrichment of the sub-Saturns relative to their parent stars vs. the planet to star mass ratio. Planets are color-coded by their envelope mass fractions. The dotted line corresponds to the correlation found in Thorngren et al. (2016) for massive planets $M_P \approx 30$–$3000\,M_\oplus$.
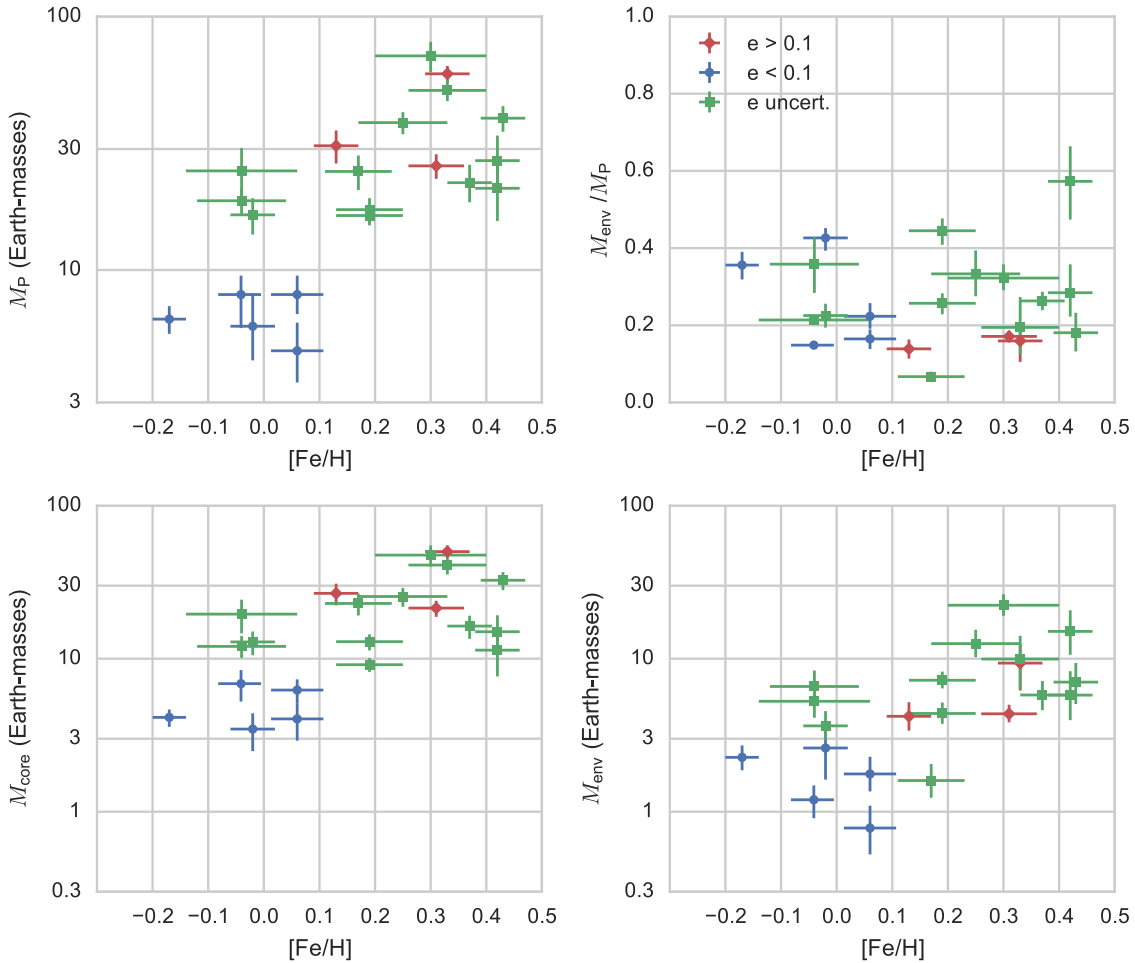
Figure 13. Same as Figure 15 but showing planet mass (M_P), envelope fraction (M_{env}/M_P), core mass (M_{core}), and envelope mass (M_{env}) as a function of stellar metallicity, [Fe/H]. We observe a correlation between metal-rich host stars and more massive sub-Saturns. The host star metallicity does not correlate with f_{env}, suggesting that disk metallicity is not the only factor that affects the final admixture of envelope and solids that comprise these planets.

In Table 7, we also included the measured eccentricities, when available. We broke the sample into low ($e < 0.1$), moderate ($e > 0.1$), and poorly constrained eccentricities. In order for a planet to be included in the low/moderate eccentricity bins, its entire 1σ eccentricity confidence interval must be below/above 0.1. Planets with eccentricity upper

Figure 15. Panels (a)–(d) show the planet mass (M_P), core mass fraction (M_{core}/M_P), core mass (M_{core}), and envelope mass (M_{env}) as a function of the number of detected planets in the system. The X-coordinates of each planet has been offset for legibility. The most massive sub-Saturns tend to reside in low-multiplicity systems.

limits or constraints straddling 0.1 fall in the poorly constrained category. These different eccentricity categories are color-coded in Figures 11, 13, and 15.

We observed that the highest-mass planets were often the only detected planet in the system. Figure 15 shows M_P, f_{env}, M_{core}, and M_{env} as a function of the total number of detected planets in the system. There is a steady decline in the mass of sub-Saturns as overall multiplicity increases. The planets with moderate eccentricities are confined to apparently single systems. These high-mass singles could originally have had neighbors, but were in a dynamically unstable architecture.

Such instabilities would eventually lead to close encounters and planet–planet scattering. Because these planets are so deep in the potential wells of their host stars, these scattering events would likely lead to mergers as opposed to ejections from the system. The maximum velocity a planet can impart to its neighbor is the escape velocity,

$$v_{esc} = 11.2 \text{ km s}^{-1} \left(\frac{M_P}{M_\oplus}\right)^{1/2} \left(\frac{R_P}{R_\oplus}\right)^{-1/2},$$

and if v_{esc} is smaller than the orbital velocity,

$$v_{orb} = 30 \text{ km s}^{-1} \left(\frac{M_\star}{M_\odot}\right)^{1/2} \left(\frac{a}{1 \text{ au}}\right)^{-1/2},$$

single scattering events cannot lead to ejections. For the sub-Saturns[21] in Table 7, $v_{esc}/v_{orb} \approx 0.1$–0.3. Any previous dynamical instabilities would likely lead to planet mergers, increasing their total mass. The present-day eccentricities of the more massive sub-Saturns may be a relic of previous scattering and merging events.

It is worth considering the biases associated with the different techniques by which planet mass and eccentricity are measured and whether they could be responsible for the observed mass–multiplicity–eccentricity trends. TTV measurements require multiplanet systems and thus do not contribute to any points in the $N_P = 1$ bin in Figure 15. Constraining $e < 0.1$ is challenging with RVs given that one is trying to measure slight deviations from sinusoidal RV curves. Therefore, limitations of the RV and TTV techniques might explain why there are no single planets with secure eccentricity measurements of <0.1.

However, these observational biases cannot explain why planets in multiplanet systems are low mass and preferentially circular. Previous studies (e.g., Weiss & Marcy 2014) have noted that planets with TTV mass measurements are typically less massive than planets with RV mass measurements. TTVs, however, are not blind to high-mass planets; such planets

---

[21] We have excluded Kepler-413 b, because it is a circumbinary planet with more complex criteria for ejection.

would produce *larger* TTVs. The lack of high-mass, high-eccentricity planets in multiplanet systems is likely the result of dynamical instabilities. Planets in such systems would likely perturb one another and merge, resulting in high-mass planets in low-multiplicity systems.

6. Conclusions

We presented RV measurements of four systems hosting sub-Saturn planets observed by the *K2* mission: K2-27, K2-32, K2-39, and K2-108. These RVs enabled mass measurements of 16% or better and detailed analysis of the planetary heavy-element fraction. Despite the similar sizes of the planets, their masses range from 16 to 60 $M_{\oplus}$, implying widely different core and envelope masses. Despite the differences in the masses of these planets, the fraction of their mass in H/He is similar $\approx 80\%$. This trend is seen in the population of ≈ 20 sub-Saturns with well-measured masses.

Sub-Saturns as a class of planets show a remarkable diversity in mass $M_P = 6$–$60\,M_{\oplus}$, with little dependence on planet size. We observe a strong correlation between stellar metallicity and planet mass. This implies that metal-rich disks produce more, or more massive, cores. Finally, we observe a tendency of the most massive sub-Saturns to have moderate eccentricities and to reside in apparently single systems. Future observational and theoretical work will further illuminate these mysterious planets, absent in our own solar system.

Software: Numpy/Scipy (Van Der Walt et al. 2011), Matplotlib (Hunter 2007), Pandas (McKinney 2010), Astropy (Astropy Collaboration et al. 2013), emcee (Goodman & Weare 2010; Foreman-Mackey et al. 2013), SME (Brewer et al. 2015), isochrones (Morton 2015), k2sc (Aigrain et al. 2015), batman (Kreidberg 2015), radvel (https://github.com/California-Planet-Search/radvel), k2phot (https://github.com/petigura/k2phot).

References

Aigrain, S., Hodgkin, S. T., Irwin, M. J., Lewis, J. R., & Roberts, S. J. 2015, MNRAS, 447, 2880
Akeson, R. L., Chen, X., Ciardi, D., et al. 2013, PASP, 125, 989
Batygin, K., Laughlin, G., Meschiari, S., et al. 2009, ApJ, 699, 23
Bodenheimer, P., Hubickyj, O., & Lissauer, J. J. 2000, Icar, 143, 2
Bonomo, A. S., Sozzetti, A., Lovis, C., et al. 2014, arXiv:1409.4592
Bordé, P., Bouchy, F., Deleuil, M., et al. 2010, A&A, 520, A66
Borucki, W. J., Koch, D., Basri, G., et al. 2010a, Sci, 327, 977
Borucki, W. J., Koch, D. G., Brown, T. M., et al. 2010b, ApJL, 713, L126
Brewer, J. M., Fischer, D. A., Basu, S., Valenti, J. A., & Piskunov, N. 2015, ApJ, 805, 126
Brewer, J. M., Fischer, D. A., Valenti, J. A., & Piskunov, N. 2016, ApJS, 225, 32
Buchhave, L. A., Latham, D. W., Johansen, A., et al. 2012, Natur, 486, 375
Butler, R. P., Vogt, S. S., Marcy, G. W., et al. 2004, ApJ, 617, 580
Ciardi, D. R., Beichman, C. A., Horch, E. P., & Howell, S. B. 2015, ApJ, 805, 16
Cochran, W. D., Fabrycky, D. C., Torres, G., et al. 2011, ApJS, 197, 7
Cosentino, R., Lovis, C., Pepe, F., et al. 2012, Proc. SPIE, 8446, 84461V
Crane, J. D., Shectman, S. A., Butler, R. P., et al. 2010, Proc. SPIE, 7735, 53
Crossfield, I. J. M., Ciardi, D. R., Petigura, E. A., et al. 2016, ApJS, 226, 7
Cumming, A., Butler, R. P., Marcy, G. W., et al. 2008, PASP, 120, 531
Cutri, R. M., Skrutskie, M. F., van Dyk, S., et al. 2003, yCat, 2246, 0
Dai, F., Winn, J. N., Albrecht, S., et al. 2016, ApJ, 823, 115
Deming, D., Harrington, J., Laughlin, G., et al. 2007, ApJL, 667, L199
Dotter, A., Chaboyer, B., Jevremović, D., et al. 2008, ApJS, 178, 89
Eastman, J., Gaudi, B. S., & Agol, E. 2013, PASP, 125, 83
Foreman-Mackey, D., Hogg, D. W., Lang, D., & Goodman, J. 2013, PASP, 125, 306
Fressin, F., Torres, G., Charbonneau, D., et al. 2013, ApJ, 766, 81
Gavrilov, S. V., & Zharkov, V. N. 1977, Icar, 32, 443
Goldreich, P., & Soter, S. 1966, Icar, 5, 375
Goodman, J., & Weare, J. 2010, Communications in Applied Mathematics and Computational Science, 5, 65
Hartman, J. D., Bakos, G. Á., Kipping, D. M., et al. 2011, ApJ, 728, 138
Horch, E. P., Howell, S. B., Everett, M. E., & Ciardi, D. R. 2012, AJ, 144, 165
Howard, A. W., & Fulton, B. J. 2016, PASP, 128, 114401
Howard, A. W., Johnson, J. A., Marcy, G. W., et al. 2010, ApJ, 721, 1467
Howard, A. W., Marcy, G. W., Bryson, S. T., et al. 2012, ApJS, 201, 15
Howard, A. W., Marcy, G. W., Fischer, D. A., et al. 2014, ApJ, 794, 51
Howell, S. B., Sobeck, C., Haas, M., et al. 2014, PASP, 126, 398
Huber, D., Bryson, S. T., Haas, M. R., et al. 2016, ApJS, 224, 2
Huber, D., Carter, J. A., Barbieri, M., et al. 2013, Sci, 342, 331
Hubickyj, O., Bodenheimer, P., & Lissauer, J. J. 2005, Icar, 179, 415
Hunter, J. D. 2007, CSE, 9, 90
Isaacson, H., & Fischer, D. 2010, ApJ, 725, 875
Jontof-Hutter, D., Lissauer, J. J., Rowe, J. F., & Fabrycky, D. C. 2014, ApJ, 785, 15
Kolbl, R., Marcy, G. W., Isaacson, H., & Howard, A. W. 2015, AJ, 149, 18
Kostov, V. B., McCullough, P. R., Carter, J. A., et al. 2014, ApJ, 784, 14
Kreidberg, L. 2015, PASP, 127, 1161
Lainey, V., Jacobson, R. A., Tajeddine, R., et al. 2017, Icar, 281, 286
Lecavelier Des Etangs, A. 2007, A&A, 461, 1185
Lee, E. J., & Chiang, E. 2015, ApJ, 811, 41
Lissauer, J. J. 1993, ARA&A, 31, 129
Lissauer, J. J., Jontof-Hutter, D., Rowe, J. F., et al. 2013, ApJ, 770, 131
Lissauer, J. J., Marcy, G. W., Rowe, J. F., et al. 2012, ApJ, 750, 112
Lopez, E. D., & Fortney, J. J. 2014, ApJ, 792, 1
Lopez, E. D., Fortney, J. J., & Miller, N. 2012, ApJ, 761, 59
Mamajek, E. E. 2009, in AIP Conf. Ser. 1158 Exoplanets and Disks: Their Formation and Diversity, ed. T. Usuda, M. Tamura, & M. Ishii (Melville, NY: AIP), 3
Marcy, G. W., & Butler, R. P. 1992, PASP, 104, 270
Marcy, G. W., Isaacson, H., Howard, A. W., et al. 2014, ApJS, 210, 20
Mardling, R. A., & Lin, D. N. C. 2004, ApJ, 614, 955
Mayor, M., Pepe, F., Queloz, D., et al. 2003, Msngr, 114, 20
McKinney, W. 2010, in Proc. 9th Python in Science Conf., ed. S. van der Walt & J. Millman, 51, http://conference.scipy.org/proceedings/scipy2010/mckinney.html
Mills, S. M., Fabrycky, D. C., Migaszewski, C., et al. 2016, Natur, 533, 509

Mordasini, C., Alibert, Y., Benz, W., & Naef, D. 2008, in AIP Conf. Ser. 398, Extreme Solar Systems, Giant Planet Formation by Core Accretion, ed. D. Fischer et al. (Melville, NY: AIP), 235

Morton, T. D. 2015, Isochrones: Stellar Model Grid Package, Astrophysics Source Code Library, ascl:1503.010

Murray, C. D., & Dermott, S. F. 1999, Solar System Dynamics (Cambridge: Cambridge Univ. Press)

O'Toole, S. J., Jones, H. R. A., Tinney, C. G., et al. 2009, ApJ, 701, 1732

Ofir, A., Dreizler, S., Zechmeister, M., & Husser, T.-O. 2014, A&A, 561, A103

Owen, J. E., & Wu, Y. 2013, ApJ, 775, 105

Bakos, G. Á., Penev, K., Bayliss, D., et al. 2015, ApJ, 813, 111

Petigura, E. A., Howard, A. W., Lopez, E. D., et al. 2016, ApJ, 818, 36

Petigura, E. A., Howard, A. W., & Marcy, G. W. 2013, PNAS, 110, 19273

Pollack, J. B., Hubickyj, O., Bodenheimer, P., et al. 1996, Icar, 124, 62

Rasmussen, C. E., & Williams, C. K. I. 2005, Gaussian Processes for Machine Learning (Cambridge, MA: MIT Press)

Astropy Collaboration, Robitaille, T. P., Tollerud, E. J., et al. 2013, A&A, 558, A33

Rogers, L. A. 2015, ApJ, 801, 41

Schwarz, G. 1978, AnSta, 6, 461

Sinukoff, E., Howard, A. W., Petigura, E. A., et al. 2016, ApJ, 827, 78

Telting, J. H., Avila, G., Buchhave, L., et al. 2014, Astronomische Nachrichten, 335, 41

Thorngren, D. P., Fortney, J. J., Murray-Clay, R. A., & Lopez, E. D. 2016, ApJ, 831, 64

Tittemore, W. C., & Wisdom, J. 1989, Icar, 78, 63

Tittemore, W. C., & Wisdom, J. 1990, Icar, 85, 394

Toomre, A. 1964, ApJ, 139, 1217

Bakos, G. Á., Torres, G., Pál, A., et al. 2010, ApJ, 710, 1724

Valenti, J. A., Butler, R. P., & Marcy, G. W. 1995, PASP, 107, 966

Van Der Walt, S., Colbert, S. C., & Varoquaux, G. 2011, arXiv:1102.1523

Van Eylen, V., Albrecht, S., Gandolfi, D., et al. 2016a, arXiv:1605.09180

Van Eylen, V., Nowak, G., Albrecht, S., et al. 2016b, ApJ, 820, 56

Vanderburg, A., & Johnson, J. A. 2014, PASP, 126, 948

Vogt, S. S., Allen, S. L., Bigelow, B. C., et al. 1994, Proc. SPIE, 2198, 362

Weiss, L. M., & Marcy, G. W. 2014, ApJL, 783, L6